nature communications

Article

https://doi.org/10.1038/s41467-025-57048-6

Identification of splenic IRF7 as a nanotherapy target for tele-conditioning myocardial reperfusion injury

Received: 6 May 2024

Accepted: 6 February 2025

Published online: 24 February 2025

Check for updates

A list of authors and their affiliations appears at the end of the paper

The sequestration of nanoparticles by mononuclear phagocyte system is a challenge for the use of nanotherapy for treating cardiovascular diseases due to the conventionally perceived loss of therapeutic potency. Here, we revitalize cardiovascular nanotherapy by unlocking an alternative route in which nanomedicines are redirected to the spleen, leveraging its potential as a highly efficient and targeted site for remote conditioning, or tele-conditioning myocardial reperfusion injury. The theoretical foundation underpinning is the splenogenic nature of recruited monocytes upon myocardial reperfusion in the acute stage, which is confirmed through murine heterotopic spleen transplantation. Single-cell RNA-seq analysis identifies IRF7 as a pivotal mediator in the spleen-heart communication network that is initially induced in the spleen and orchestrates functional changes in myocardial macrophages. Spleen-related induction of IRF7 is also valid in human myocardial reperfusion scenarios. In addition, in a murine preclinical model of male mice, temporal inhibition of splenic IRF7 through the designed spleen-targeting erythrosome engineered with the targeting peptide RP182, termed as STEER nanoparticles, mitigates the acute-stage innate immune responses and improves the cardiac function in the long term. In contrast, systemic inhibition, genetic knockout of IRF7 or absolute depletion of splenic monocytes does not have therapeutic benefits, indicating the superiority of nanoparticle-based targeted treatment. These findings establish the spleen as a naturally favored site for nanoparticle-based treatments, offering promising avenues for managing myocardial reperfusion injury.

Modulating myocardial reperfusion injury is crucial for improving the long-term prognosis of patients with ischemic cardiovascular events. Nanotherapies are emerging as a promising adjunct intervention approach for regulating reperfusion injury owing to their advantages in convenience, flexibility, noninvasiveness, and precise targeting potency[1,2]. However, the critical challenge still lies in insufficient and heterogeneous nanoparticle (NP) accumulation in the heart. Conventional design principles for addressing this issue solely emphasize the increase in in situ cardiac accumulation after systemic NP administration, exploiting various strategies, including ligand conjugation, surface modification, and size optimization[3–6]. With limited success in increasing cardiac accumulation, this classical principle of design faces inevitable barriers posed by mononuclear phagocyte system (MPS) clearance and sequestration, hindering the targeted delivery of nanomaterials to the injured myocardium and presenting substantial challenges for the translation and clinical utilization of nanomaterials[7,8].

Previous studies, including our own, have sought to promote cardiac tropism in NPs by leveraging immune cells as natural carriers with the inherent capability to infiltrate and localize to the lesion sites[3,9–12]. Among all the leukocytes, monocytes, which are potential "target frameworks", have drawn increasing amounts of attention due to their high mobility, propensity for innate phagocytosis, and extensive

e-mail: zehua.liu@helsinki.fi; zq11607@rjh.com.cn; xiaofengye@hotmail.com

participation in immune response regulation. However, the number of circulating monocytes is highly dynamic and accounts for only 2–8% of total blood leukocytes[6]. Moreover, monocytes residing in the MPS, or monocyte reservoir, outnumber their equivalents in the blood pool, and are continuously activated and mobilized upon traumatic challenges[13]. Along with the spontaneous sequestration of NPs by MPS, these features render the MPS a favorable alternative function-of-site for maximizing the therapeutic potential of monocyte-targeted nanotherapy. However, to exploit such a strategy, two fundamental issues need to be addressed. Although previous studies have identified the spleen as a major monocyte reservoir upon acute myocardial infarction (MI)[14], studies of myocardial ischemia-reperfusion (IR), which is associated with distinct pathological and biological features from those of MI, are relatively rare. Second, a broad therapeutic strategy simply adopting the concept of "anti-inflammation" has shown to be therapeutically insufficient for myocardial IR[15]; therefore, an improved understanding of how to selectively target destructive factors while preserving beneficial immune homeostasis may generate more promising results.

The present study aimed to address whether NPs sequestered by MPS, which are conventionally regarded as "off-target" and have been actively avoided, can be re-exploited for the purpose of modulating myocardial reperfusion injury. To this end, we first explored and confirmed the spleen as an acute monocyte reservoir upon myocardial reperfusion. We subsequently identified IRF7 as a major mediator that regulates the cardio-splenic immune network. After confirming the human relevance of IRF7 in a clinical setting, we further examined the detailed biological function of IRF7 to provide a theoretical foundation for the NP treatment scheme. Finally, we developed a spleen-targeting nanosystem, termed STEER, which was tested in a murine model of myocardial IR. By abandoning the concept of evading MPS scavenging for enhanced in situ cardiac accumulation, we aim to offer a previously unappreciated therapeutic avenue to mitigate cardiac damage.

Results

Splenic monocytes mobilize to the heart after myocardial IR injury

The presence of macrophages in the healthy adult heart is limited, and the spleen and bone marrow are traditionally recognized as the primary sources of monocytes following injury or biological stimulation[14,16]. Therefore, we first assessed the predominant source of recruited macrophages following cardiac IR injury. The enumeration of monocytes in different tissues at 1 day after myocardial IR was first evaluated by flow cytometry. While the blood showed an increase in monocytes, the number of monocytes decreased in the spleen but remained constant in the bone marrow (Fig. 1a), potentially suggesting that the recruitment of macrophages during acute stages post-IR may be predominantly contributed by the spleen. We also observed that the number of monocytes in the subcapsular red pulp of the spleen significantly decreased (Fig. 1b), partially indicating the mobilization of monocytes from the spleen after myocardial IR. We further confirmed that activated splenic monocytes were recruited to the injured myocardium. We developed an experiment by labeling splenic cells with near-infrared fluorescent dye (DiD) via intrasplenic injection, and the mice were sequentially subjected to a sham or IR operation. One day after the operation, we observed an elevated fluorescent signal in the heart only in the IR group, but this phenomenon was not observed in the sham group (Fig. 1c), indicating that remote splenic cells may mobilize into the injured heart. To correlate the temporal genetic profile alterations, we performed whole-transcriptome sequencing of the spleen at 4 h and 24 h post-myocardial IR. The results indicated early activation of genes associated with leukocyte migration at 4 h, and these levels then returned to levels similar to those observed in the healthy spleen (sham-operated) at 24 h (Fig. 1d, Supplementary Data 1, 2), indicating a rapid and dynamic genetic response of splenic leukocyte mobilization following myocardial IR.

Finally, robust evidence that splenic monocytes mobilize to the injured myocardium was derived from a mouse model of heterotopic spleen transplantation (Supplementary Fig. 1). The model involved wild-type C57BL/6J mice that underwent splenectomy. These mice subsequently received spleen transplants from ROSA$^{mT/mG}$ mice and were then subjected to myocardial IR (Fig. 1e, f). We observed significant enrichment and infiltration of Ly6c$^+$tdTomato$^+$ monocytes in the injured myocardium, indicating that a proportion of the infiltrated monocytes originated from the spleen (Fig. 1g). Taken together, these results confirm that the spleen contributes to cardiac-mobilized monocytes after myocardial IR injury.

Splenectomy exhibits pleiotropic effects on myocardial IR

After confirming that the spleen contributes to the cardiac-recruited monocytes following myocardial IR, we proceeded to investigate the potential biological impact of the spleen in mediating the IR injury. We adopted a well-established splenectomy model to fully abrogate the participation of splenic monocytes or other splenic immune cells without interfering with other monocyte pools, including those in the bone marrow and blood[14]. Mice with or without splenectomy were subjected to 1 h of ischemia, and we separately assessed the extent of myocardial IR injury at 1 day, 1 week, and 6 weeks after reperfusion. These time points are typically used to evaluate the acute stage, short-term consequences, and long-term consequences of cardiac IR injury (Fig. 2a). As expected, splenectomy significantly reduced the infiltration of monocytes in the infarct region after 24 h of reperfusion. Although we also observed markedly reduced recruitment of neutrophils (Fig. 2b), at 24 h after reperfusion, the total number of blood neutrophils in the different groups (with or without splenectomy) was not significantly different (Supplementary Fig. 2). This may be attributed to the fact that the neutrophils are dominantly produced by bone marrow, and these outnumber the neutrophil population in the spleen[17]. Moreover, monocytes are known as major mediators of neutrophil infiltration and mobilization at lesion sites[18,19]. Therefore, the reduced number of neutrophils may be partly due to the reduced enrichment of monocytes within the infarct region. Splenectomy markedly reduced the IR-induced myocardial infarct size from 45.58% to 32.81% of the area at risk, and the area at risk was similar between the two groups (Fig. 2c). These findings suggest that the ablation of splenic monocytes or other immune cells may ameliorate the acute-stage IR injury. In the short-term, splenectomy significantly improved cardiac ventricular performance after IR by 1 w after reperfusion, as indicated by an increase in ejection fraction (Fig. 2d, e), fractional shortening (Supplementary Fig. 3a) and reduced fibrotic area compared to spleen$^+$ controls (Fig. 2g). However, a comparable left ventricular end-diastolic volume (LVEDV) and left ventricular end-systolic volume (LVESV) were observed between the two groups (Fig. 2e). Notably, we also observed a significant decrease in macrophage infiltration in the myocardium at 1 w post reperfusion (Fig. 2f).

These findings indicate the need for further investigations with prolonged reperfusion time. The robust and persistent recruitment of various myeloid cells upon myocardial IR contributes to both destructive and reparative processes and is proposed to be a major mediator of long-term cardiac remodeling and heart failure. Notably, the observed functional benefits of splenectomy did not persist after 6 w of reperfusion. In fact, cardiac function deteriorated, as the ejection fraction and fractional shortening decreased, and left ventricular dilation increased (Fig. 2h, i, Supplementary Fig. 3b). This profile was also associated with a decrease in left ventricle wall thickness and an increase in the fibrotic area (Fig. 2j). Taken together, these results indicate that the depletion of the spleen, which fully eliminates splenic monocytes, has pleiotropic effects on myocardial IR consequences.

https://doi.org/10.1038/s41467-025-57048-6

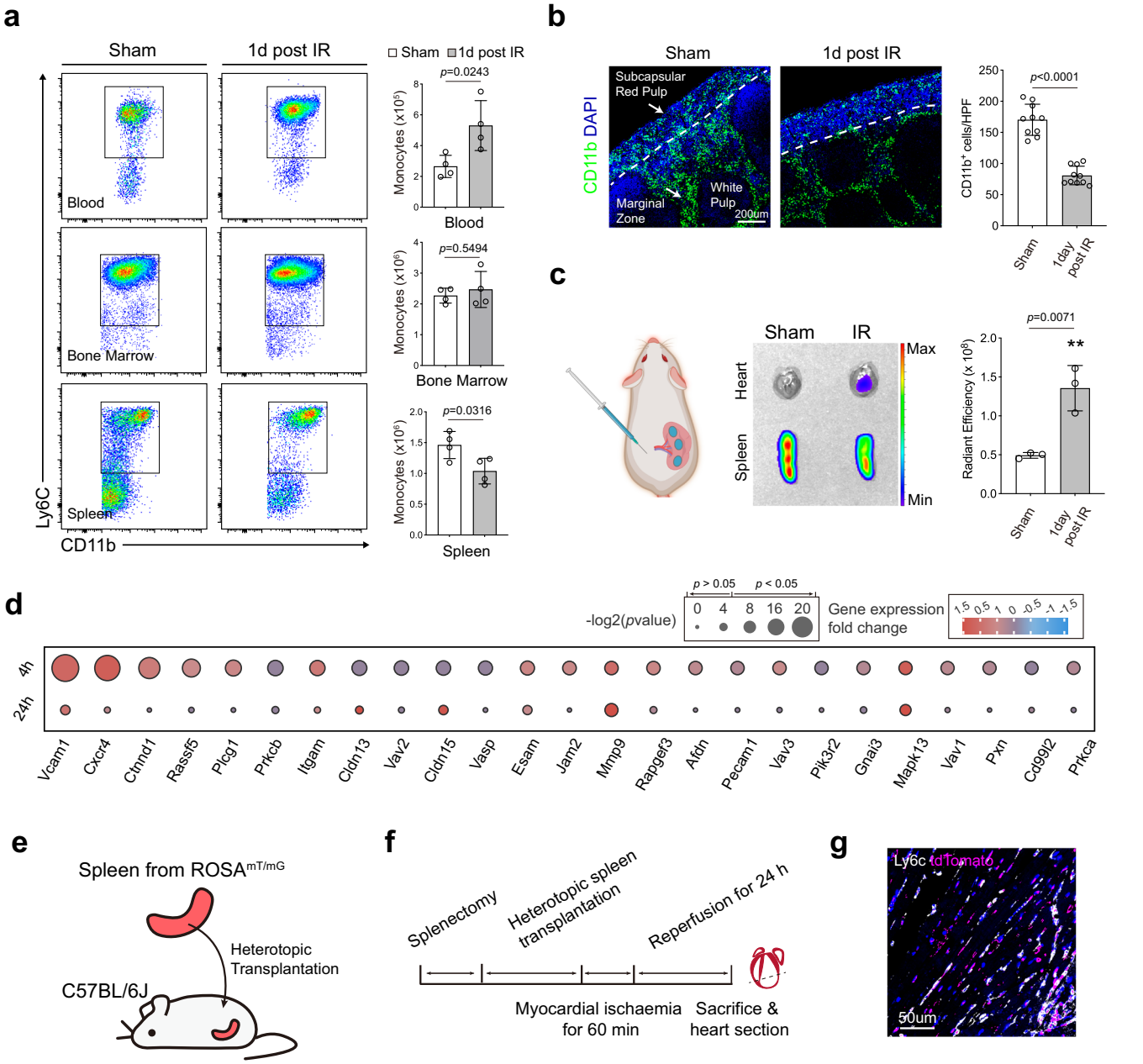

Fig. 1 | Splenic monocytes mobilize to the heart after myocardial IR injury. **a** Flow cytometric analyses of immune cells isolated from the blood, bone marrow and spleen of sham-operated mice and mice subjected to ischemia-reperfusion (IR) at 1 day post-reperfusion. The total number of monocytes in the blood, bone marrow (unilateral fibula and tibia) and spleen were separately quantified ($n = 4$ mice per group). **b** Immunofluorescence images of splenic sections stained with CD11b (green) and DAPI (blue) from sham-operated mice and mice subjected to IR at 1 day post-reperfusion. Quantification of $CD11b^+$ cells was based on 10 high power fields. **c** Mice were injected intrasplenically with DiD prior to sham or IR procedures. The heart and spleen were separately collected at 1 d post-reperfusion and subjected to fluorescent imaging, and the radiant efficiency of heart from different groups was quantified ($n = 3$ mice per group). The schematic was created with Biorender.com (https://BioRender.com/j61p721). **d** Dot plots showing the splenic transcriptional profiles of selected genes associated with leukocyte transendothelial migration. Spleens from mice subjected to myocardial IR at 4 or 24 h post-reperfusion were compared separately to spleens from the sham group. **e**, **f** Schematic illustration of quantitative tracking of splenic monocytes recruited to the heart after the induction of IR. **g** Heart section stained with Ly6c (white), tdTomato (pink) and DAPI (blue) from C57BL/6 J mice after spleen transplantation. These experiments were repeated independently three times with similar results. The data are expressed as mean ± s.d. Statistical analyses were conducted by unpaired two-tailed Student's *t*-test. Source data are provided as a Source Data file.

Splenectomy alters the proportions of macrophage subclusters after myocardial IR

To gain detailed knowledge of the macrophage signatures and spleen-related macrophage alterations associated with myocardial IR, we characterized the types and states of immune cells involved in myocardial IR in mice with or without splenectomy, using single-cell RNA-Seq (scRNA-seq). At 24 h post reperfusion, the left ventricle (lesioned myocardium) was collected and processed into a single-cell suspension. $CD45^+$ cells were separated by magnetic cell sorting from splenectomised mice and sham-operated mice (Supplementary Fig. 4a). A total of 7897 quality-control-positive cells were captured, clustered and visualized in t-distributed stochastic neighbor embedding (t-SNE) plots (Supplementary Fig. 4b). At 24 h after myocardial IR, macrophages constituted a substantial proportion of the cell population in mouse hearts, as they accounted for 38.94% of the total $CD45^+$ cells. Among the other leukocytes, neutrophils accounted for 48.86%

https://doi.org/10.1038/s41467-025-57048-6

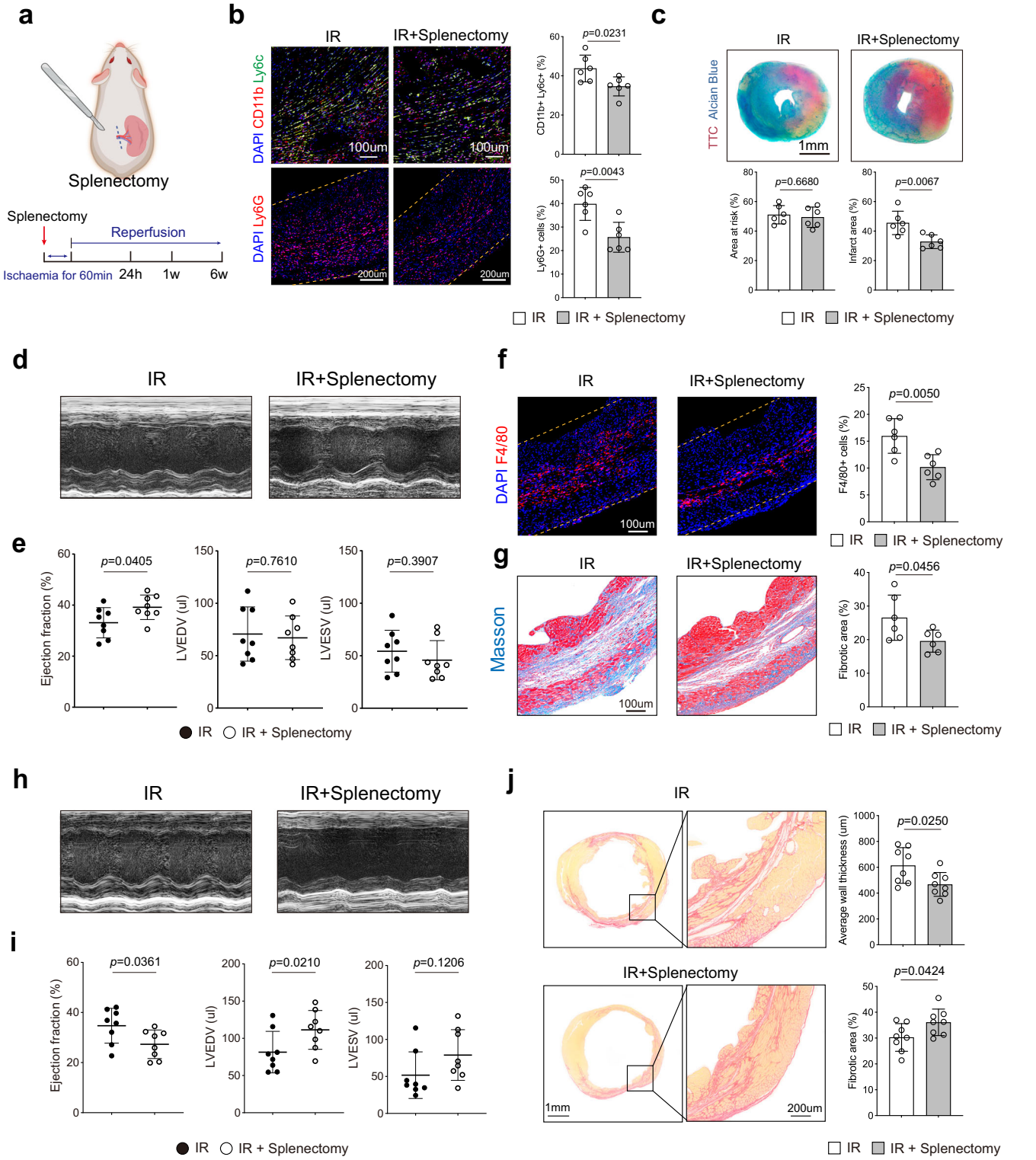

of the total cells; these were followed by dendritic cells (6.28%), B cells (2.72%), T cells (1.85%) and NK cells (1.35%) (Supplementary Fig. 4b–e).

For a deeper understanding of macrophage subtypes post-IR, we conducted subclustering analysis using scRNA-seq data, resulting in the identification of 6 distinct subclusters (Supplementary Fig. 5a, b). Notably, Mac1 and Mac2 predominated over the other macrophage subtypes, as they accounted for 66.70% of the total macrophages (Fig. 3a). Interestingly, the most striking difference induced by splenectomy was the drastic increase in the Mac2 cluster and the concomitant decrease in the Mac1 cluster (Fig. 3b). Overall, we confirmed that the splenectomy significantly altered cardiac macrophage patterns upon myocardial IR, not only in absolute number but also in phenotypic heterogeneity.

Splenectomy induces functional bias in macrophages

We hypothesize that detailed transcriptional profiling of Mac1 and Mac2 may offer insights into the biological function of splenic monocytes in mediating myocardial IR. To this end, we first assessed whether Mac1 and Mac2 represent different maturation statuses. We performed a trajectory analysis via the Monocle R package, where Ly6c2^{hi}

Fig. 2 | Splenectomy exhibits pleiotropic effects on myocardial IR. a Schematic illustration of the experimental design. Mice with sham surgery or splenectomy, with preserved bone marrow and blood monocyte pools, were separately subjected to 60 min of cardiac ischemia followed by 24 h, 1 w or 6 w of reperfusion for subsequent analyses. The schematic was created with Biorender.com (https://BioRender.com/j61p721). **b** Representative images and quantification of co-immunofluorescent staining of CD11b (red), Ly6c (green), Ly6G (red), and DAPI (blue) in heart specimens at 24 h of reperfusion with or without splenectomy ($n = 6$ mice per group). **c** Representative alcian blue/TTC staining and quantification of AAR/LV area and infarct/AAR ratios ($n = 6$ mice per group). TTC, 2,3,5-triphenyltetrazolium chloride; AAR, area at risk; LV, left ventricle. **d**, **e** Representative M-mode echocardiographic images and corresponding quantifications of ejection fraction, LVEDV, and LVESV from splenectomised or sham-operated mice at 1w after myocardial IR injury ($n = 8$ mice per group). LVEDV, left ventricle end-diastolic volume; LVESV, left ventricle end-systolic volume. **f** Representative images and quantification of immunofluorescent staining of F4/80 (red) and DAPI (blue) in heart specimens at 1 w of reperfusion with or without splenectomy ($n = 6$ mice per group). **g** Masson trichrome staining depicts a reduced fibrotic region from splenectomised mouse group at 1 w after IR comparing to the sole IR group ($n = 6$ mice per group). **h**, **i** Representative M-mode echocardiographic images and corresponding quantifications of ejection fraction, LVEDV and LVESV from splenectomised or sham-operated mice at 6 w after myocardial IR injury ($n = 8$ mice per group). **j** Sirius red staining and corresponding quantification at 6 weeks after myocardial IR injury ($n = 8$ mice per group). The data are expressed as mean ± s.d. Statistical analyses were conducted by unpaired two-tailed Student's *t*-test. Source data are provided as a Source Data file.

subclusters were set as the root of the trajectory (Fig. 3c, Fig. S5c). The expression levels of early macrophage markers (Ccr2, Ly6c2, Chil3, and Clec4e) and late macrophage markers (Rgs10 and Trem2) were separately plotted to assess the maturation status of each macrophage subcluster (Fig. 3d). We observed that Mac1 and Mac2 diverged relatively early in the pseudo-time; however, they shared a similar temporal pattern. These findings suggest that the major difference may be attributed to the transcriptional signature rather than the maturation status. To obtain a preliminary understanding of the phenotypic function of Mac1 and Mac2, we separately filtered the marker genes for Mac1 and Mac2 and subjected them to Kyoto Encyclopedia of Genes and Genomes (KEGG) analysis. We compared the functional patterns of Mac1 and Mac2 across 7 major aspects: cell migration, cell motility, antigen processing and presentation, endocytosis, regulation of type I interferon production, cytokine production, and leukocyte activation (Fig. 3e). The gene enrichment levels related to migratory cascades, such as cell migration and cell motility, were more prominent in Mac2. However, Mac1 was associated with a distinct functional pattern indicative of a pronounced phagocytic and inflammatory stimulatory effects, such as endocytosis and cytokine production. This finding is consistent with the results obtained from gene set variation analysis (GSVA, Supplementary Fig. 6). Together with the findings of proportional alterations in macrophages observed via scRNA-seq, our data suggest that abrogation of the spleen impeded proinflammatory cascades within the recruited macrophages without hindering their influx to the lesioned sites.

Identification of IRF7 as a mediator in spleen-heart communication network

To elucidate the mechanisms underlying the observed reduction in Mac1 and increase in the proportion of Mac2 cells, we used an integrative approach by searching for the top significant differentially expressed genes (DEGs) ($P < 0.05$, with a fold change > 1.5 between two subclusters). We found that conventional criteria could not be used to determine which cluster, Mac1 or Mac2, is more proinflammatory. For instance, although Mac1 exhibited higher transcriptional levels of chemokines such as Ccl12 and Pf4, the expression of IL-1α/β and Ccl24 was significantly greater in Mac2 than in Mac1 (Supplementary Data 3). However, among the top 20 genes upregulated in Mac1, 13 were monocyte/macrophage-related type-I interferon-regulated genes (IRGs)[20], and the most significant gene was IRF7 (Fig. 3f). Although IRF7 is recognized as a key regulator of type I interferon-dependent immune responses[21], its exact function in myocardial IR remains unclear. We hypothesize that the Mac1 is a type-I interferon-stimulated macrophage subcluster, and that, considering the significantly reduced proportion of Mac1 in the myocardium after splenectomy, IRF7 may function as a major regulator of the spleen-heart inflammatory network. To confirm this, we first validated the location of primary IRF7 induction. We separately explored the time-dependent changes in IRF7 expression in the spleen and injured myocardium after myocardial IR (Fig. 3g). Notably, splenic IRF7 expression levels increased as early as 1 h after reperfusion, whereas the peak change in IRF7 expression in the injured myocardium occurred after 4 h. These findings indicate that IRF7 expression did not rise simultaneously in both organs but instead was first induced in the spleen. To further understand the distinct roles of IRF7 and other IFN-I regulators, we also investigated IRF3, another well-established IFN-I regulator, in both the spleen and injured myocardium during the acute phase following IR injury. Unlike IRF7, IRF3 expression in the injured myocardium remained unchanged during the acute stages following reperfusion (Supplementary Fig. 7a). Splenic expression of IRF3 showed a modest induction at 1 h post-reperfusion, paralleling the early induction of IRF7. However, its induction was notably lower compared with that of IRF7 (Supplementary Fig. 7b).

We next investigated the potential paracrine or telecrine mechanisms driving IRF7 induction and sought to identify the stimulatory factors. We collected the serum at 1 h after reperfusion and intravenously injected it into healthy mice. IR serum treatment increased IRF7 expression in the spleen, which was similar to the levels observed in mice with myocardial IR. Furthermore, heat-denatured IR serum showed a splenic IRF7 upregulation efficiency comparable to that of the pristine IR serum, whereas this phenomenon was not detected in DNase-treated or RNase-treated IR serum (Supplementary Fig. 7c). These results demonstrate that splenic IRF7 is induced in a telecrine manner after myocardial IR, and that the relevant factors in IR serum are nucleic acids (DNA and RNA).

To elucidate the involvement of splenic IRF7 in the myocardial IR injury, we assessed IRF7 expression in the injured myocardium of both spleen$^+$ and spleen$^-$ mice at various reperfusion time points following IR. The expression levels of IRF7 in the injured myocardium were consistently greater in spleen$^+$ mice than in the spleen$^-$ mice at all time points. Interestingly, we observed a clear two-peak pattern in the myocardial expression of IRF7 upon IR. A second peak emerged at 3 days after reperfusion and gradually decreased (Fig. 3h). The wound healing process after ischemic myocardial injury is biphasic, initialized by an inflammatory phase, which usually occurs within minutes to a few hours after damage and is typically characterized by leukocyte infiltration, cytokine production, and dead cell clearance[22]. Over the course of 3 to 7 days, the inflammatory phase progressed to a reparative phase, which leads to inflammation resolution and scar formation[23,24]. Notably, two IRF7 expression peaks arose in both the inflammatory and reparative phases, potentially indicating that IRF7 participates in both two phases and plays a role in macrophage phenotype switching.

To further characterize the expression pattern of IRF7 across various splenic immune cell subsets, we conducted flow cytometry analysis to assess the expression levels of IRF7 at 1 h post-myocardial IR, corresponding to the peak expression of IRF7 in the spleen (Fig. 3g). As illustrated in Supplementary Fig. 8, IRF7 was predominantly expressed in Ly6C^{high} and Ly6C^{low} monocytes. Conversely, its expression level was much lower in neutrophils, B cells, T cells, and NK cells. Despite substantial IRF7 expression observed in DCs, monocytes significantly outnumbered DCs in the spleen (approximately a 5-fold difference). We

https://doi.org/10.1038/s41467-025-57048-6

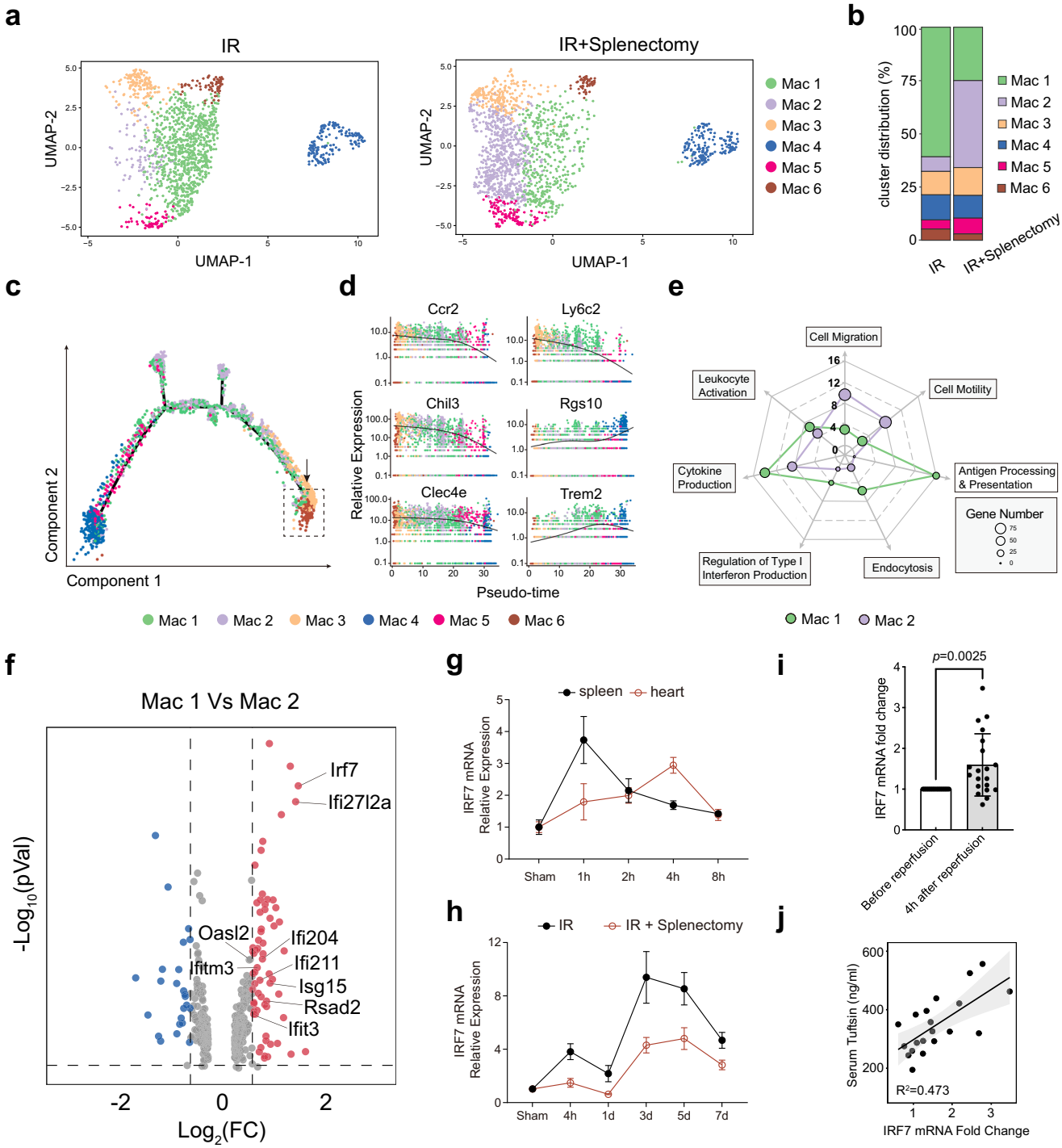

Fig. 3 | Single-cell RNA-Seq identifies IRF7 as a mediator in regulating cardiac macrophage heterogenicity after IR. a Two-dimensional uniform manifold approximation and projection (UMAP) visualization of macrophages from sham and splenectomised mice at 24 h after myocardial IR identified 6 macrophage sub-clusters after unsupervised clustering. **b** Proportions of each sub-cluster in sham versus splenectomy groups. **c** Pseudo-time analysis investigating the path and progress of individual cells undergoing differentiation. Ly6c2^{hi} monocytes were set as the root of the trajectory. The scale indicates the temporal status, from dark brown (Ly6c2^{hi} monocytes) to dark blue (Late macrophages). **d** Spline plots showing expression of typical markers associated with early (Ccr2, Ly6c2, Chil3, Clec4e) and late (Rgs10, Trem2) macrophage sub-clusters. **e** Radar plot illustrating the heterogeneous function of Mac1 and Mac2 regarding cell migration, cell motility, antigen processing and presentation, endocytosis, regulation of type I interferon production, cytokine production and leukocyte activation. The dot size represents the gene number enriched in the corresponding KEGG term, and the distance from the dot to center represents false discovery rate (FDR, -log2FDR) of the corresponding KEGG term. **f** Volcano plots showing differentially expressed genes between Mac1 and Mac2. **g** Splenic and cardiac IRF7 expression at different time points after myocardial IR ($n = 4$ mice per time point, except $n = 3$ at 1 h in the spleen group and $n = 3$ at 4 h in the heart group.). **h** Cardiac IRF7 expression in sham or splenectomised mice at different time points after myocardial IR ($n = 3$ mice at each time point). **i** IRF7 expression in blood monocytes from 20 patients with acute myocardial infarction, sampled upon emergency department arrival and ~4 h after PCI. PCI, percutaneous coronary intervention. **j** Scatter plot illustrating the correlation between the serum tuftsin level and the fold change of IRF7 mRNA expression in monocytes. The grey area represents the 95% confidence interval. The data are expressed as mean ± s.d. Statistical analyses were conducted by paired two-tailed Student's *t*-test. Source data are provided as a Source Data file.

further characterized the expression pattern of IRF7 across various blood immune cell subsets following myocardial IR. As shown in Supplementary Fig. 9, similar to its expression profile in splenic immune cells, IRF7 was also predominantly expressed in Ly6C^{high} and Ly6C^{low} monocytes. IRF7 expression was much lower in neutrophils, B cells, T cells, and NK cells. In conclusion, in the context of myocardial IR, IRF7 is expressed primarily in blood monocytes and splenic monocytes/DCs.

To confirm that the increase in IRF7 after myocardial IR is also valid in humans, we evaluated the IRF7 expression levels in blood monocytes from 20 patients who experienced acute myocardial infarction and subsequently underwent percutaneous coronary intervention (PCI) for coronary artery revascularization, which is one of the most common clinical myocardial IR scenarios. We collected the monocytes from each patient upon arrival at the emergency department and 4 h after PCI. The IRF7 expression level in monocytes was significantly increased after PCI (Fig. 3i). To further elucidate the correlation between the IRF7 expression and the spleen function, the pre-PCI serum level of tuftsin, an immunomodulatory peptide exclusively derived from the spleen that serves as an indicator of the immunological potency of the spleen[25], was tested for each patient. Linear regression analysis revealed that the extent of IRF7 expression in monocytes was strongly associated with the serum level of tuftsin detected by ELISA ($R^2 = 0.473$, Fig. 3j). Collectively, our findings indicate that IRF7 induction upon myocardial IR is valid in humans and is positively correlated with spleen function.

IRF7 regulates both the proinflammatory activation and phenotypic transition of macrophages

Considering the correlation between the expression pattern of IRF7 and the temporal trajectory of the inflammatory cascade, together with the aforementioned pleiotropic effects of spleen on cardiac IR, we speculated that IRF7 has a pleiotropic role in regulating macrophage functions and phenotypes. To this end, we generated IRF7 knockout (IRF7-/-) mice by deleting the exon 5-10 of the IRF7 gene via CRISPR/Cas9, and their nullizygosity was confirmed by DNA blot analyses (Supplementary Fig. 10). Bone marrow-derived macrophages (BMDMs) were isolated from both IRF7(−/−) mice and wild type (WT) mice for further investigation. IRF7 plays a central role in regulating type I interferon-dependent immune responses. Indeed, compared with WT BMDMs, IRF7(−/−) BMDMs exhibited a significant decrease in IFN-β secretion upon exposure to lipopolysaccharide (LPS, Fig. 4a). Moreover, the production of the chemoattractant Cxcl10 and the proinflammatory cytokine interleukin-6 was only moderately, but with statistical significance, reduced in IRF7(−/−) BMDMs (Fig. 4a). The expression of interferon-stimulated genes, including IFN-α1, IFN-β1, ISG15, and IFIT1, was also significantly reduced in IRF7(−/−) BMDMs upon LPS stimulation (Supplementary (Fig. 11a). These findings indicated that IRF7 promotes a pro-inflammatory response in macrophages, primarily through, but not limited to the activation of type-I interferon pathways. We further evaluated M1-to-M2 phenotypic switch using a previously established method involving prolonged LPS exposure (24 h)[26]. The transcriptional levels of Nos2 and Arg1, which are typical M1 and M2 macrophage markers, respectively, were both significantly lower in IRF7(−/−) BMDMs than in wild-type BMDMs (Fig. 4b). Consistently, flow cytometry also revealed that the expression levels of both the M1 macrophage marker CD80 and M2 macrophage marker CD206 were decreased in IRF7(−/−) BMDMs (Fig. 4c, d, Supplementary Fig. 11b). Overall, compared to that in WT macrophages, type-I interferon responses were significantly reduced in IRF7(−/−) macrophages, and the M1-to-M2 phenotype transition was also notably impaired.

IRF7 deficiency ameliorates short-term reperfusion injury but does not improve long-term cardiac function

To determine the functional significance of IRF7 in determining myocardial IR prognosis, we compared the cardiac function after myocardial IR between IRF7(−/−) and wild type mice at different reperfusion times. At 1 week after myocardial IR, IRF7 knockout mice exhibited protective effects comparable to those seen in splenectomised mice. The ejection fraction and fractional shortening were increased, while the LVEDV and LVESV were substantially decreased, indicating attenuated global left ventricular dysfunction (Fig. 4e, f, Supplementary Fig. 12a). However, when we extended the observation period to 6 weeks after reperfusion, the cardioprotective effects of IRF7 KO were abolished, with no difference in ejection fraction, fractional shortening, LVESV or LVEDV between in IRF7 (−/−) mice and WT mice (Fig. 4g, h, Supplementary Fig. 12b). Moreover, there was no significant change in the fibrotic area or left ventricular wall thickness in IRF7 (−/−) mice, compared to WT mice at 6 weeks after reperfusion (Fig. 4i–k). Notably, in contrast to mice that underwent splenectomy, IRF7(−/−) mice exhibited no further deterioration in cardiac function, suggesting that other signaling pathways in the spleen may also participate in reparative processes after myocardial IR. Therefore, although IRF7 deficiency partly prevents the heart from reperfusion injury at an early stage, the protective effect of IRF7 deficiency was not preserved during prolonged observation. These results indicate that IRF7 plays a restricted dual role in the progression of myocardial reperfusion injury.

HS-38 is a potential small-molecule inhibitor of IRF7

Considering the divergent molecular functions of IRF7 in myocardial IR, transient inhibition of spleen IRF7 at the early stage of IR, rather than long-term systemic inhibition, may better exert protective effects on the myocardium. Small interfering RNA (siRNA)-based IRF7 inhibition has been utilized; however, gene knockdown by siRNA can last 5-7 days[27–29], which is not suitable for the current treatment settings. Therefore, we turned to small-molecule inhibitors. Specific IRF7 inhibitors are currently unavailable. Nonetheless, a previous study identified death-associated protein kinase 1 (DAPK1) as a specific IRF7-interacting protein[30], and since knockdown of DAPK1 inhibited the transcription and expression of IRF7, we hypothesized that HS38, a selective inhibitor of DAPK1, could effectively inhibit IRF7 expression. The effect of HS38 on IRF7 inhibition was first tested in RAW264.7 cells stimulated with IFN-β. Treatment with 10 μM HS38 significantly reduced the IRF7 transcription, whereas a further increase in the HS38 concentration did not cause a further decrease in IRF7 expression (Fig. 5a). This phenomenon was consistent with the protein expression pattern (Fig. 5b). To simulate myocardial IR in vitro, hypoxic-reoxygenation conditioned media from human cardiomyocytes (AC16 cell line) were collected and added to the human monocytic cell line THP-1 with or without pretreatment with 10 μM HS38. Flow cytometry revealed that HS38 pretreatment reduced the CD80 expression in IR medium-challenged THP-1 cells (Fig. 5c, Supplementary Fig. 13). Moreover, HS38 significantly reduced the expression of IFN-α1 and IFN-β1 in THP-1 cells upon IFN-β stimulation (Supplementary Fig. 14a), demonstrating that HS38 pretreatment could attenuate the type I interferon responses of macrophages. Meanwhile, HS38 failed to further inhibit type I interferon responses in IRF7(−/−) BMDMs (Supplementary Fig. 14b), suggesting that the effect from HS38 was IRF7-dependent.

Construction of spleen-targeting nanoerythrosomes engineered with RP182 (STEER)

After validating the therapeutic potential of splenic intervention for modulating myocardial IR and the successful inhibition of IRF7 by HS38, we next constructed spleen-targeting NPs to achieve the envisioned purposes. To this end, we aimed to adopt erythrocyte-derived materials, or erythrosomes, as major building blocks for vehicle construction due to their inherent spleen targeting capability as well as satisfactory biosafety[31,32]. To enhance intrinsic spleen tropism, we functionalized erythrosomes with vascular homing peptides[33]. To identify spleen-homing peptides, we used in vivo peptide phage playoff technology, which allows

https://doi.org/10.1038/s41467-025-57048-6

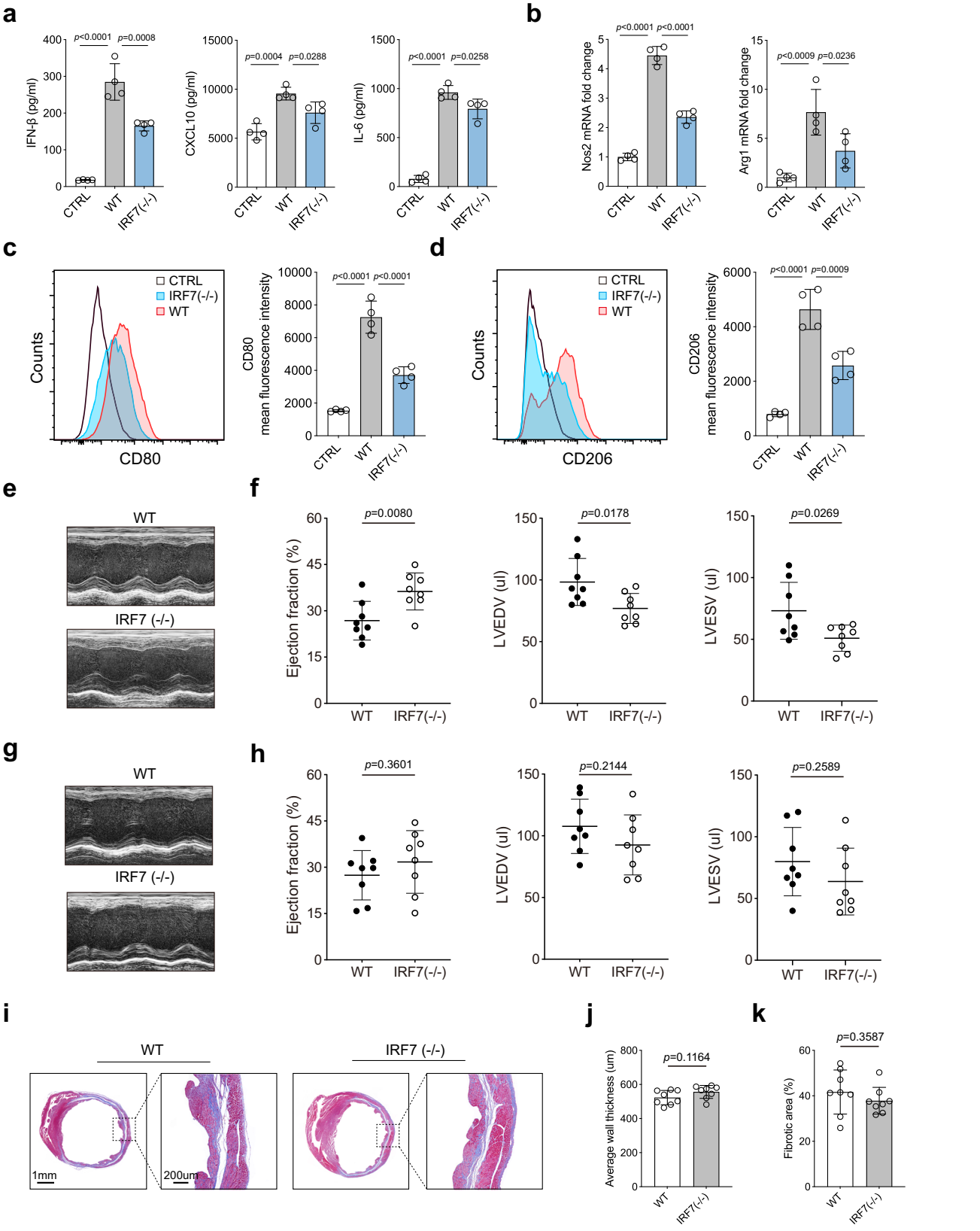

for the head-to-head comparative evaluation of the biodistribution of multiple peptide phages in the same animal[34]. In addition, the inclusion of positive and negative phages provides quality control for homing experiments and allows comparison of independent playoff studies. Mice were dosed with an equimolar mixture of T7 bacteriophages engineered to display 27 different vascular homing peptides. The representation of each phage in the input mixture and in spleen and control tissue (lung, brain, liver) samples was determined via Ion Torrent high-throughput DNA sequencing (Fig. 5d). In vivo phage playoff studies showed that the RP182 peptide-displaying phages outperformed other phage candidates in terms of spleen enrichment (Fig. 5e).

Fig. 4 | IRF7 deficiency protects against acute myocardial IR injury but impairs macrophage phenotype switch. a levels of pro-inflammatory cytokines including IFN-β, CXCL10, IL-6 in the culture supernatants of BMDMs from wild-type C57BL/6 J mice and IRF7(−/−) mice after LPS (500 ng/ml) stimulation for 4 h ($n = 4$ independent experiments). **b** Nos2 and Arg1 expression in BMDMs from wild-type C57BL/6 J mice and IRF7(−/−) mice after LPS (500 ng/ml) stimulation for 24 h ($n = 4$ independent experiments). **c** Representative histograms of CD80 expression in BMDMs from WT and IRF7(−/−) mice after 24 h of LPS stimulation, with corresponding mean fluorescence intensity quantification ($n = 4$ independent experiments). **d** Representative histograms of CD206 expression in BMDMs from WT and IRF7(−/−) mice after 24 h of LPS stimulation, with corresponding mean fluorescence intensity quantification ($n = 4$ independent experiments). **e** Representative M-mode echocardiographic images from wild type or IRF7(−/−) mice at 1 w after IR. **f** Quantifications of ejection fraction, LVEDV and LVESV of wild type or IRF7(−/−) mice at 1 w after IR ($n = 8$ mice per group). LVEDV, left ventricle end-diastolic volume; LVESV, left ventricle end-systolic volume. **g** Representative M-mode echocardiographic images from wild type or IRF7(−/−) mice at 6 w after IR. **h** Quantifications of ejection fraction, LVEDV and LVESV of wild type or IRF7(−/−) mice at 6 w after IR ($n = 8$ mice per group). **i** Representative images of Masson trichrome staining of wild type and IRF7(−/−) mice. **j**, **k**, Quantitative measurement of average wall thickness and fibrotic area (%) of wild type and IRF7(−/−) mice ($n = 8$ mice per group). The data are expressed as mean ± s.d. Data were analyzed by one-way ANOVA with Tukey's post hoc test. Source data are provided as a Source Data file.

Furthermore, based on its potential receptor, RP182 can either directly bind to RelB to enhance the interaction with monocytes or indirectly facilitate monocyte recognition and phagocytosis by blocking CD47 on erythrosomes[35]. Therefore, we developed a nanosystem termed Spleen-Targeting Erythrosome Engineered with RP182 (STEER, Fig. 5f). The hydrodynamic diameter of the pristine erythrosomes increased from 126 to 136 nm after DSPE-PEG fusion to obtain PEGylated erythrosomes, which was further increased to 146 nm with surface functionalization of RP182 to construct STEER NPs (Fig. 5g). Accordingly, the surface ζ-potential of the STEER NPs was -18 mV, which was slightly greater than that of the bare erythrosomes (-25 mV) and PEGylated erythrosomes (−24 mV) (Supplementary Fig. 15). The loading degree of HS38 in the STEER NPs reached 20.60 ± 2.80% (w/w, relative to the protein content in erythrosomes), with an encapsulation efficiency of 84.60 ± 3.00%. After successful encapsulation of HS38 (STEER-HS38), the size increased to 161 nm, whereas the surface ζ-potential only exhibited a negligible change from −18 mV to −17 mV (Fig. 5g, Supplementary Fig. 15). The polydispersity index (PDI) of the bare erythrosomes, PEGylated erythrosomes, STEER NPs and STEER-HS38 NPs were consistently less than 0.30, indicating a homogenous population of NPs (Supplementary Fig. 16a). Moreover, the NPs remained stable in 20% fetal bovine serum over 4 h, indicating good serum stability (Supplementary Fig. 16b,c). STEER-HS38 NPs displayed a uniform and spherical structure when visualized by transmission electron microscopy (TEM) (Fig. 5h, i). The encapsulation and distribution profiles of HS38 in the STEER NPs were further analysed using energy dispersive X-ray spectroscopy (EDX). Element mapping of phosphorus (the most abundant element in phospholipids), sulfur (commonly observed in membrane proteins), and chlorine (representative element in HS38) overlapped (Fig. 5j–l) with the resultant compositional profile (Fig. 5m), suggesting that HS38 was embedded in the phospholipid bilayer of STEER NPs. To evaluate the safety of STEER-HS38, PBS or STEER-HS38 (3.5 mg/kg) was intravenously injected into healthy mice. Biomarkers of liver and kidney function showed no significant differences between the PBS group and the STEER-HS38 group (Supplementary Fig. 17b). Major organs, including the liver, heart, lung, kidney and spleen, exhibited no signs of toxicity (Supplementary Fig. 17a), indicating a high safety profile for STEER-HS38.

Biodistribution of STEER NPs

To validate the enhanced monocyte targeting and binding efficiency endowed by RP182 modification, we compared the interactions between human monocytes (THP-1 cells) with PEGylated erythrosomes or STEER NPs, in which the hydrophobic dye fluorescein was incorporated as an indicator for flow cytometry analysis. After 4 h of incubation, compared with unmodified PEGylated erythrosomes, STEER NPs significantly enhanced cellular binding, as evidenced by the percentage of positive cells and the mean fluorescent intensity (MFI) (Fig. 6a–c), indicating that RP182 modification promoted monocyte interaction.

We then examined the spleen targeting capability of STEER NPs in vivo. The infrared fluorescence dye DiD was encapsulated in STEER (STEER-DiD) or PEGylated erythrosomes for in vivo visualization. STEER-DiD NPs showed substantially greater accumulation in the spleen at 4 h after intravenous injection than free DiD (dispersed in 2% Pluronic F68) or PEGylated erythrosomes (Fig. 6d). The dissected spleens in the STEER-HS38 group exhibited the highest fluorescence intensity among all groups, although a strong fluorescent signal was also detected in the liver (Fig. 6e). Comparative analysis revealed that, STEER-DiD induced a 5.8-fold and 1.9-fold greater spleen targeting index (as determined by total spleen radiant efficiency / total liver radiant efficiency) compared with free DiD and PEGylated erythrosomes, respectively (Fig. 6f).

To explore the interaction between STEER NPs and various immune cell subsets in the spleen, spleens were harvested at 1 h post-myocardial IR and intravenous injection of STEER-DiO or DiO formulated with an FDA-approved stabilizer (Pluronic F68, 2%, w/v). The enhanced spleen-targeting ability of STEER NPs was evidenced by a significantly greater percentage of DiO-positive cells in the spleen than that of free DiO, as shown in Fig. 6g and Supplementary Fig. 18. Notably, $Ly6C^{high}$ monocytes and DCs exhibited the highest DiO-positive percentages when administered with STEER-DiO (Supplementary Fig. 18), underscoring major cellular uptake of STEER NPs by these cells. Consistent with the splenic IRF7 expression profile depicted in (Supplementary Fig. 8), which highlights $Ly6C^{high}$ monocytes and DCs as the major sources for IRF7 expression, these findings suggest that STEER NPs may serve as potent drug delivery systems for attenuating splenic IRF7 expression. We also examined the interaction between STEER NPs and various blood immune cell subsets, STEER-DiO NPs predominantly colocalized with blood $Ly6C^{hi}$ and $Ly6C^{low}$ monocytes (Supplementary Fig. 19). Taken together, our findings show that, compared with free drugs, our designed STEER NP system effectively promotes spleen accumulation and is effectively recognized by monocytes in both the blood and spleen, suggesting that this system is a promising drug delivery platform for the efficient inhibition of IRF7.

Finally, to confirm the enhanced delivery of HS38 to the spleen by STEER NPs, we conducted pharmacokinetic investigations and assessed the organ distribution of free HS38 and STEER-HS38. Free HS38 (dispersed in 0.5% or 2% F68, w/v), or STEER-HS38, was intravenously injected into Wistar rats at an HS38 concentration of 1.75 mg/kg. The circulation clearance of free HS38 was negatively correlated with the concentration of F68 (Supplementary Fig. 20, Supplementary Table 1). Nonetheless, free HS38 dispersed in 2% F68 exhibited comparable plasma pharmacokinetic parameters to STEER-HS38, making it suitable for further comparison of the organ distribution of HS38. 1 h after the injection, key organs (liver, spleen, lung and kidney) were harvested to evaluate the organ distribution of HS38, and the results demonstrated a 10-fold increase in splenic HS38 accumulation after STEER-HS38 administration (Supplementary Fig. 21). These findings confirm the superior splenic targeting and accumulation capabilities of STEER NPs.

https://doi.org/10.1038/s41467-025-57048-6

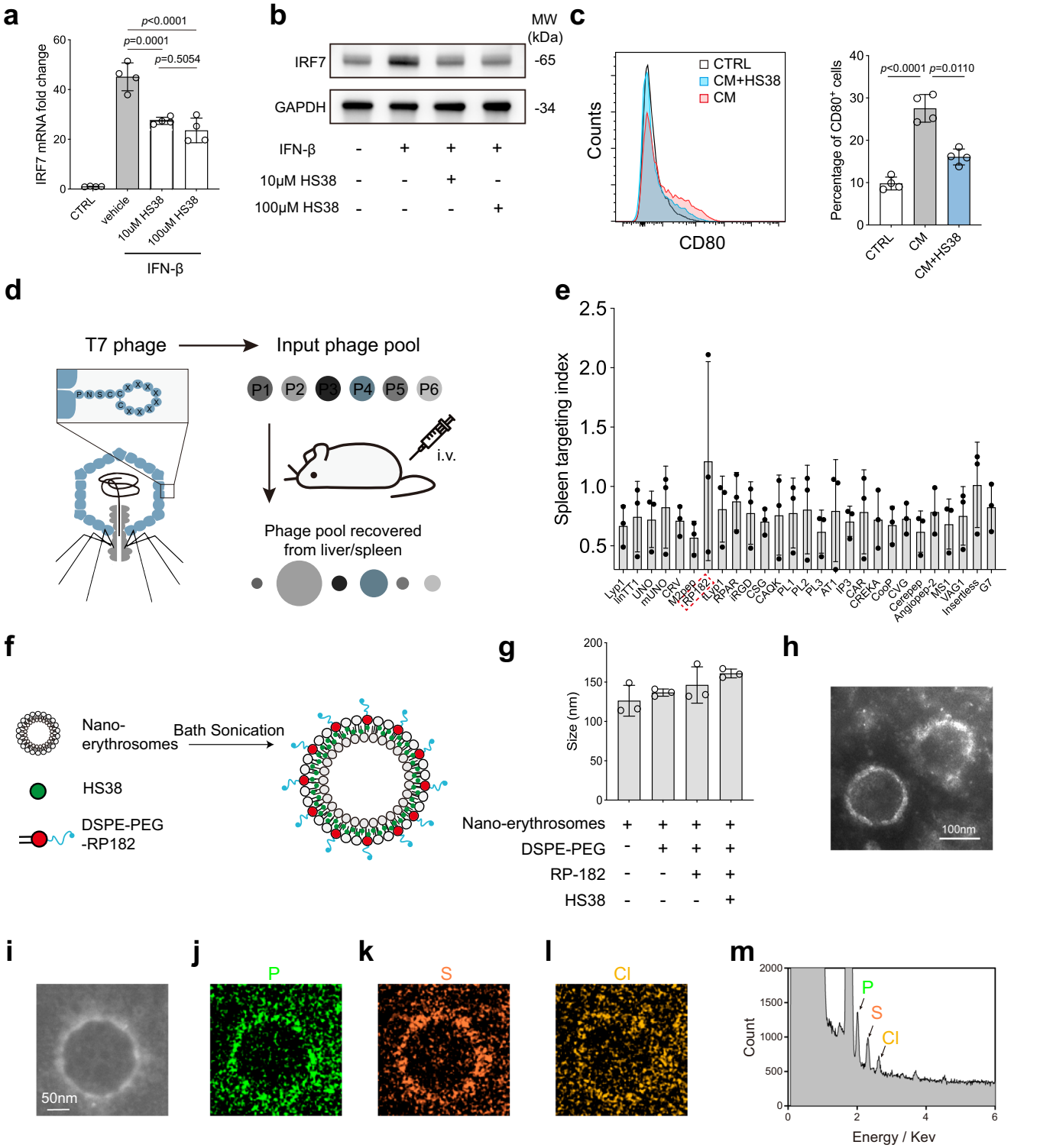

Fig. 5 | Construction and characterization of STEER-HS38. a IRF7 expression in RAW 264.7 cells after IFN-β (10 ng/ml) stimulation and treatment with 10 μM or 100 μM HS38 for 24 h ($n = 4$ independent experiments). **b** Western blot analysis of IRF7 in RAW 264.7 cells upon different treatment. These experiments were repeated independently three times with similar results. **c** Representative histograms of flow cytometric analysis of THP-1 cells after 24 h incubation with hypoxic-reoxygenation conditioned medium (H/R CM) from AC16 cells, with corresponding quantification of CD80+ cell percentage ($n = 4$ independent experiments). **d** Schematic representation of in vivo peptide phage playoff technology for assessing the target selectivity of known homing peptides. **e** Spleen targeting index of each peptide. The red dotted box marks RP-182 ($n = 3$ mice per group). **f** Schematic representation of fabricating STEER-HS38. **g** Hydrodynamic diameter of bare nano-erythrosomes, PEGylated erythrosomes, PEGylated erythrosomes/DSPE-PEG-RP182 and STEER-HS38, measured by dynamic light scattering ($n = 3$ independent experiments). **h, i** TEM images of STEER-HS38. EDX elemental mapping image of (**j**) phosphorus, (**k**) sulfur and (**l**) chlorine of an individual STEER-HS38 nanoparticle. These experiments were repeated independently three times with similar results. **m** Elemental scanning profiles of the STEER-HS38. The data are expressed as mean ± s.d. Data were analyzed by one-way ANOVA with Tukey's post hoc test. Source data are provided as a Source Data file.

https://doi.org/10.1038/s41467-025-57048-6

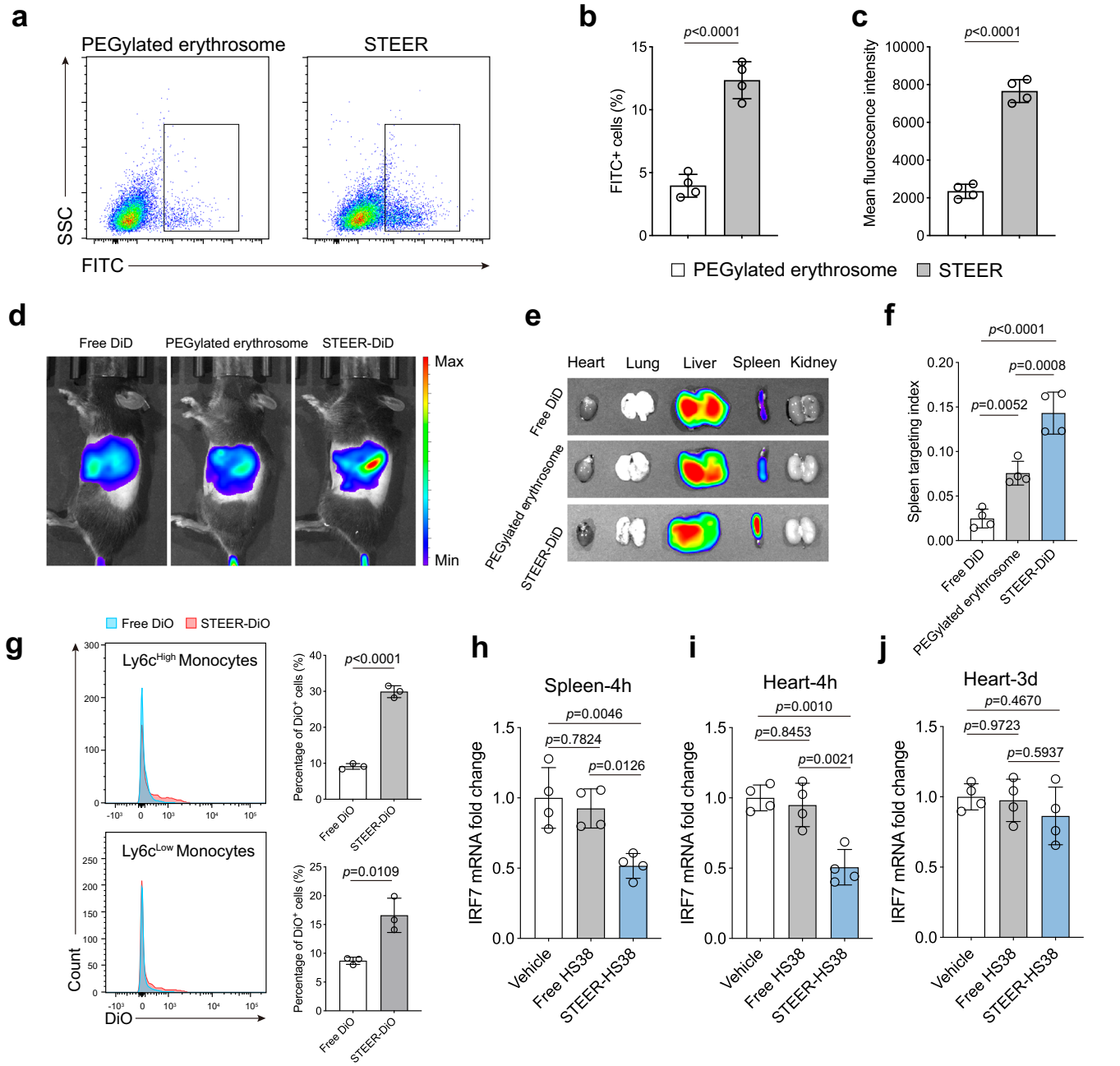

Fig. 6 | Biodistribution of STEER NPs and in vivo efficacy of STEER-HS38. a Flow cytometric analyses of THP-1 cells incubated with nano-erythrosomes and STEER NPs (labeled with fluorescein). **b** Quantification of FITC+ cells percentage and **c** Mean fluorescence intensity of THP-1 cells ($n = 3$ independent experiments). **d** Real-time fluorescence imaging of mice at 4 h after intravenous injection of Free DiD (dispersed in 2% F68), DiD-labeled PEGylated erythrosomes and STEER-DiD. **e** Ex vivo fluorescence imaging of major organs from mice at 4 h after intravenous injection of Free DiD, DiD-labeled PEGylated erythrosomes and STEER-DiD. **f** Quantification of spleen targeting index (calculated by total spleen radiant efficiency / total liver radiant efficiency) of Free DiD, DiD-labeled PEGylated erythrosomes and STEER-DiD ($n = 4$ mice per group). **g** Histograms depict flow cytometric analysis of splenic monocytes and quantification of DiO+ cells percentage in ly6c^{high} and ly6c^{low} cells. Mice were subjected to myocardial IR and intravenously injected with Free DiO (dispersed in 2% F68) or STEER-DiO, spleens were harvested 1 h later ($n = 3$ mice per group). IRF7 expression in spleens (**h**) and hearts (**i**) at 4 h after myocardial IR and intravenously injected with vehicle, free HS38 (dispersed in 2% F68) and STEER-HS38 ($n = 4$ mice per group). **j** IRF7 expression in hearts at 3 days after myocardial IR and intravenously injected with vehicle, free HS38 (dispersed in 2% F68) and STEER-HS38 ($n = 4$ mice per group). The data are expressed as mean ± s.d. Data were analyzed by unpaired two-tailed Student's *t*-test or one-way ANOVA with Tukey's post hoc test. Source data are provided as a Source Data file.

STEER-HS38 preconditioning reduces acute-stage, but not long-term, IRF7 induction

Considering the pleiotropic and temporally restricted functions of IRF7 expression, we concluded that a rational approach for myocardial reperfusion treatment involves temporary and reversible IRF7 inhibition. In this pursuit, we devised a preconditioning approach by intravenously (i.v.) injecting free HS38 (formulated with 2% F68) or STEER-HS38 at an HS38 concentration of 3.5 mg/kg, at 1 h prior to the myocardial IR process. The spleens and hearts were separately harvested at 4 h postreperfusion to evaluate the expression level of IRF7. As shown in (Fig. 6h), when subjected to myocardial IR challenge, a single injection of STEER-HS38 significantly reduced the extent of IRF7 expression in the spleen compared with that in the vehicle or free HS38 treatment. Accordingly, significantly reduced IRF7 expression was

observed solely in the heart after STEER-HS38 treatment (Fig. 6i). These findings indicate the effectiveness and superiority of STEER-HS38 in attenuating IRF7 expression during myocardial IR in both the spleen and heart on a short-term basis. Notably, free HS38 was unable to efficiently inhibit IRF7 expression in both the spleen and heart when challenged by myocardial reperfusion, which was likely due to the limited spleen accumulation, as shown in Fig. 6d–f. These findings indicate the superiority of the STEER-based therapeutic approach, which involves enhancing and selectively targeting IRF7 expression. For comparison, when we prolonged the reperfusion time to 3 days, which correlated with the second peak of IRF7 expression and may be responsible for the inflammatory transition and resolution, the inhibition of IRF7 by both HS38 and STEER-HS38 was abrogated (Fig. 6j).

Moreover, we explored the therapeutic time window of STEER-HS38 administration after the onset of myocardial infarction (MI). We evaluated the therapeutic efficacy of STEER-HS38 at three distinct time points: immediately after the initiation of MI (following the LAD ligation), 0.5 h after MI, and 1 h after MI (but prior to reperfusion). As shown in Supplementary Fig. 22a, even when administered 1 h after MI (before reperfusion), STEER-HS38 still reduced the extent of IRF7 expression in the spleen, indicating the broad therapeutic time window of STEER-HS38. Collectively, these findings demonstrated that a single STEER-HS38 injection can temporarily inhibit IRF7 expression during the acute phase but does not affect IRF7 expression in the long term.

To assess the impact of temporary IRF7 inhibition by STEER-HS38 on antiviral immune response, mice that received intravenous STEER-HS38 administration were further challenged by intraperitoneal injection of 10 μg poly(I:C) to simulate a viral challenge. Serum IgM and IgG levels after one week (Supplementary Fig. 22b) showed no significant changes compared to controls, indicating that transient IRF7 inhibition did not impair the humoral immune response.

STEER-HS38 improves myocardial reperfusion outcomes

Finally, we tested the therapeutic effects of STEER-HS38 on acute cardiac injury and long-term left ventricular remodeling after myocardial IR. As shown in (Supplementary Fig. 23), the aforementioned single-shot preconditioning by STEER-HS38 reduced macrophage and neutrophil infiltration in the injured myocardium. In contrast, the reduced infiltration of immune cells was less pronounced in the free HS38 treatment group. STEER-HS38 treatment decreased the infarct size to 19.3 ± 3.7% of the left ventricle at 24 h post-reperfusion, which was significantly lower compared with free HS38 (28.7 ± 4.0%) or no treatment (27.2 ± 3.4%) (Fig. 7a). This finding indicates that STEER-HS38 led to less myocardial necrosis and apoptosis. This conclusion was further corroborated by reductions in lactate dehydrogenase (LDH) release (Fig. 7b) and terminal-deoxynucleotidyl transferase mediated nick end labeling (TUNEL) staining (Fig. 7c) at 24 h post-reperfusion. To elucidate the transcriptional landscape in the acute stage (24 h post IR) after free HS38 or STEER-HS38 treatment, we performed RNA-seq analysis across different groups (Supplementary Fig. 24a, (Supplementary Data 4). The results demonstrated that the expression of key genes involved in inflammation, including chemokines (Ccl2, Ccl5, Ccl7, Ccl12, CXCL1, CXCL5, CXCL10, CXCL12, CXCR2 and CXCR4), pro-inflammatory cytokines (IL-1b, IL6, IL11 and TNF), cell adhesion molecules (Icam1, Icam2 and Vcam1), fibrosis progression (matrix metallopeptidases, MMPs; MMP9 and MMP14), and toll-like receptors activation (TLR4, TLR7, TLR8, TLR9, Myd88, TRAF3 and TRAF6), and most importantly, interferon stimulated genes (Isgs; ISG15, Oasl1, Oasl2, Ifit1, Ifit2, Ifit3, Ifit203, Ifit204, Rsad2, IRF3, IRF5 and IRF7), was downregulated in the STEER-HS38 treatment group, but this phenomenon was substantially less pronounced in the group treated with the free HS38. Gene Set Enrichment Analysis (GSEA) further revealed distinct patterns of gene set deactivation in the inflammatory response, fibrosis (IL-17A signaling) and apoptosis upon STEER-HS38 treatment, highlighting the potential beneficial transcriptional alterations implicated in the STEER-HS38 treatment group (Supplementary Fig. 24b). Moreover, the protein levels of two key inflammatory factors, IL-6 and IFN-b, in the injured myocardium significantly decreased after STEER-HS38 treatment (Supplementary Fig. 25). These results demonstrated that STEER-HS38 treatment can effectively reduce the acute-stage innate immune responses, exhibiting a therapeutic efficacy that surpasses that of free HS38.

The cardioprotective efficacy of STEER-HS38 was also reflected in cardiac function. At 1 week postreperfusion, the left ventricular ejection fraction recovered from 30.7 ± 7.0% (no treatment) to 38.9 ± 7.3% after STEER-HS38 treatment, while free HS38 (29.6 ± 4.8%) had no positive effect on cardiac function (Fig. 7d, e). However, no significant differences were observed in left ventricular remodeling, reflected by the LVEDV or LVESV, among the three groups at 1 week. One major drawback for systemic IRF7 deficiency is the diminished therapeutic potency in the long term. Therefore, we investigated whether the beneficial effects of STEER-HS38 preconditioning persist over an extended period. At 6 weeks postreperfusion, the enhanced cardiac function induced by STEER-HS38 treatment was still valid, as shown by the increase in the left ventricular ejection fraction and fractional shortening compared to those in free HS38-treated or untreated mice (Fig. 7f, g). In addition, the LVEDV decreased to 77.3 ± 12.9 μL in the treatment group compared with the no treatment (101.1 ± 18.9 μL) or free HS38 (97.6 ± 14.5 μL) group, indicating reduced ventricular dilation (Fig. 7g). Masson's trichrome staining revealed that the percentage of the left ventricle occupied by fibrosis was lower in STEER-HS38 treated mice, and wall thickness was also preserved (Fig. 7h–j). Taken together, these results indicate that targeted inhibition of splenic IRF7 by STEER-HS38 augments the recovery from myocardial IR injury.

Discussion

In summary, the present study highlights the concept that a substantial portion of nanomedicines sequestered by the spleen, once deemed to be therapeutically abrogated and thus have long been actively avoided, can be repurposed through precise targeting of signaling pathways and cell subsets, offering protective benefits in myocardial reperfusion injury. The implementation of this concept is based on four major conclusions obtained from the present study: 1) The spleen substantially participates in the deployment of monocytes upon myocardial IR in the acute stage, and actively engages in immune regulation in the heart. 2) A specific transcription factor, IRF7, is initially expressed in the spleen and orchestrates the immune network between the spleen and heart in a dynamic, pleiotropic manner. 3) Only temporal inhibition of splenic IRF7, but not its systemic knockout, can exert long-term cardioprotection against myocardial IR, and this precise, yet dynamic feature renders it an ideal nanotherapy target for tele-conditioning myocardial reperfusion injury; 4) The correspondingly designed and constructed nanoplatform, termed STEER-HS38, achieves the envisioned purposes with great clinical translation potency. This insight guides a selective, temporal and cell-specific therapeutic strategy to precisely target the destructive response while enhancing long-term prognosis.

Nanomedicine is emerging rapidly as a convenient and non-invasive option for targeted cardiovascular disease treatment; however, insufficient cardiac accumulation remains a challenge due to the anatomical structure, large cardiac output[4], rapid blood flow, dilution effects[36], and other biological barriers[8,37]. Previous research, including our own, exploits native monocyte infiltration to enhance cardiac NP accumulation in a "Trojan horse" manner, capitalizing on the massive influx of recruited monocytes during myocardial reperfusion injury[3,9–12]. However, this raises a crucial question: where do the recruited monocytes originate? Herein, we identify the spleen as a monocyte reservoir that mobilizes monocytes to injured myocardium in a remote manner. The spleen, as the primary site of blood filtration

https://doi.org/10.1038/s41467-025-57048-6

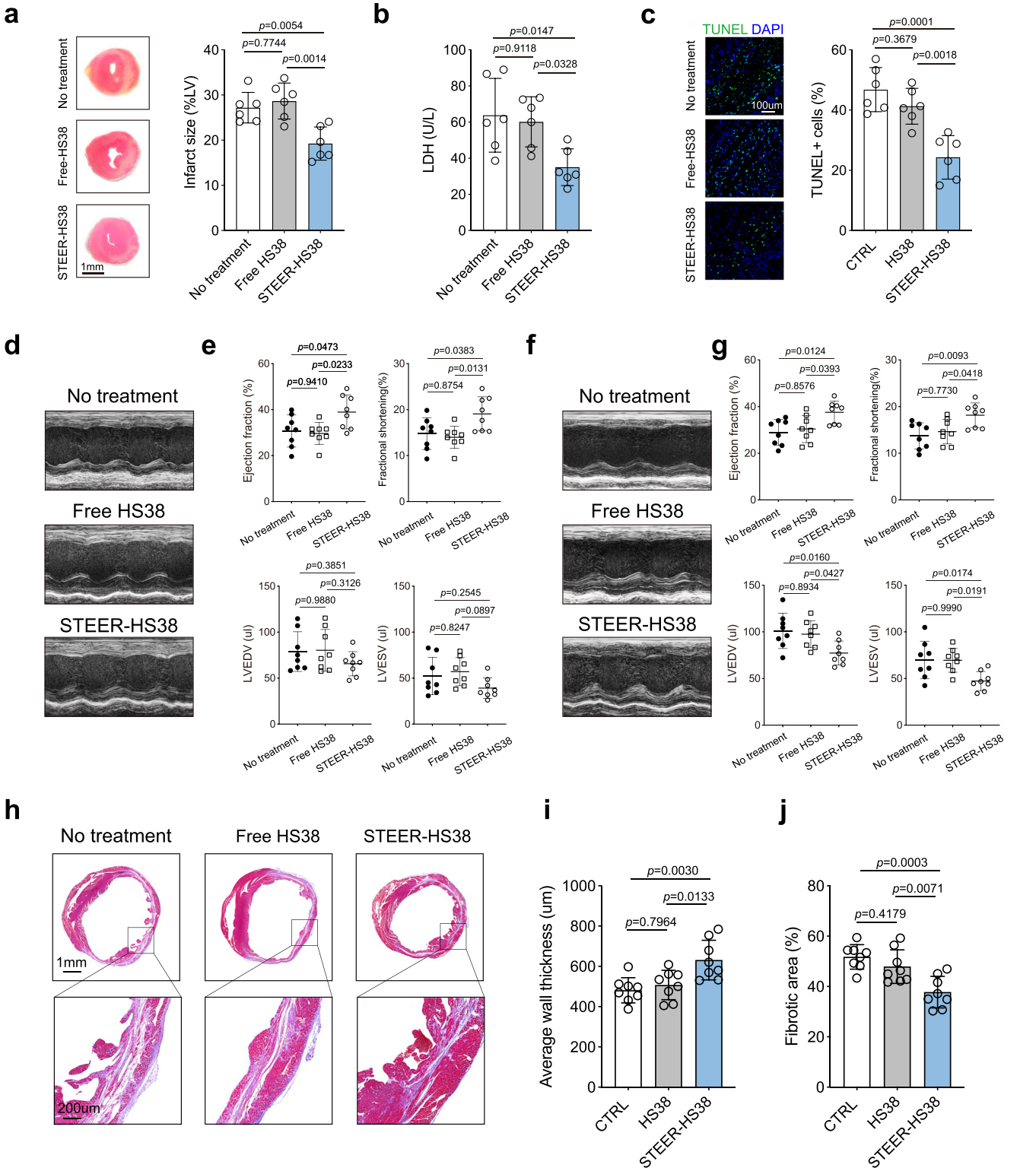

Fig. 7 | STEER-HS38 improves myocardial reperfusion outcomes. a Representative TTC-stained slices of mice hearts subjected to 60 min of ischemia followed by 24 h of reperfusion, with the administration of free HS38 (dispersed in 2% F68) or STEER-HS38, or no treatment. Quantification of infarct size according to TTC staining ($n = 6$ mice per group). **b** Serum LDH concentrations in mice at 24 h after IR injury with no treatment, free HS38 (dispersed in 2% F68) or STEER-HS38 ($n = 6$ mice per group). **c** Representative TUNEL staining of mice at 24 h after IR injury with no treatment, free HS38, or STEER-HS38 and quantification of TUNEL$^+$ cells ($n = 6$ mice per group). **d** Representative M-mode echocardiographic images from mice at 1 w after IR injury. **e** Quantifications of ejection fraction, fractional shortening, LVEDV and LVESV at 1 w after IR injury ($n = 8$ mice per group). LVEDV, left ventricle end-diastolic volume; LVESV, left ventricle end-systolic volume. **f** Representative M-mode echocardiographic images from mice at 6 w after IR injury. **g** Quantifications of ejection fraction, fractional shortening, LVEDV and LVESV at 6 w after IR injury ($n = 8$ mice per group). **h** Representative images of Masson trichrome staining of heart at 6 w after IR injury. **i**, **j** Quantitative measurement of average wall thickness and fibrotic area (%) ($n = 8$ mice per group). The data are expressed as mean ± s.d. Statistical analyses were conducted by one-way ANOVA with Tukey's post hoc test. Source data are provided as a Source Data file.

in the body[38], possesses a natural propensity to filter blood-borne molecules, rendering it a spontaneous filtration site for different types of NPs[39]. Along with its role as a key player in controlling systemic inflammation in response to sterile inflammation, the roles identified by these findings establish a robust theoretical basis for leveraging the spleen in nanotherapeutic interventions.

Extensive studies indicate that abnormally amplified inflammatory cascades have deleterious consequences in the context of sterile injury[22]. Although depletion of the spleen attenuated acute inflammatory responses in myocardial IR and preserved early-stage cardiac function, we observed a worsened prognosis with prolonged reperfusion time. This observation parallels the findings of previous studies, where splenectomy was associated with impaired left ventricular ejection fraction and the formation of a thinner scar after myocardial infarction[40]. These findings emphasize the multifaceted nature of the spleen and its significance in orchestrating the complex cellular events necessary for cardiac recovery.

We established a splenectomised murine model with preserved bone marrow and blood monocyte pools, and further subjected the mice to myocardial IR to evaluate the sole effects of splenic monocytes on the functional heterogeneity of recruited macrophages in the injured myocardium. The sequential integration of scRNA-seq provided a high-resolution interpretation of myocardial macrophage phenotype profiles and identified IRF7 as a potential mediator of macrophage heterogeneity in the lesioned myocardium. In particular, our study suggested that IRF7 expression was remotely initiated in the spleen and further shifted to the injured myocardium. Notably, we observed that IRF7 was also expressed in monocytes obtained from patients who experienced acute myocardial infarction and subsequently underwent PCI for coronary artery revascularization. The expression of IRF7 is strongly associated with the splenic functions of individuals, highlighting the translational significance of our experimental observations.

While IRF3 is typically regarded as the primary initiator of IFN-β production via TBK1-mediated phosphorylation, IRF7 functions as a feed-forward amplifier of IFN-I responses[21,41,42]. In our study, IRF3 expression remained largely unchanged in the injured myocardium during early IR, despite IRF3 also showing a modest increase in the spleen at 1 h post-reperfusion. However, its overall induction was notably lower than that of IRF7. Previous studies have referred to interruption of the type I IFN response as a potential cardioprotective strategy for myocardial infarction[43]. In the present study, we observed opposing biological effects of IRF7 at different stages. Recent studies have shown the involvement of IRF7 in macrophage polarization, specifically in promoting the proinflammatory M1 phenotype[44–46] and facilitating the resolution of inflammation through M2 phenotype polarization[26]. Consistently, we observed a two-peak pattern of IRF7 expression at both the acute inflammatory stage (as early as 1 h post-IR) and 3 days postreperfusion, which is conventionally thought to be the transition point for the macrophage phenotypic switching[47]. Although IRF7 deficiency reduced the secretion of key proinflammatory mediators, such as IFN-β, Cxcl10, and IL-6, it also impaired the polarization of macrophages from the M1 to M2 phenotype. This duality may explain the complex injury outcomes observed in IRF7(−/−) or splenectomised mice. Collectively, these findings underscore the need for temporal, IRF7-focused interventions that moderate early inflammation while preserving later reparative functions.

In the pursuit of targeted IRF7 inhibition, siRNAs have been frequently utilized[48], however, their sustained effects, which last up to 5-7 days, do not align with our objectives. As an alternative approach, we turned to small molecule inhibitors, which are known for their relatively short-term impact. However, specific inhibitors of IRF7 are unavailable at present, necessitating the selection of proper targets to achieve the indirect inhibition of IRF7. DAPK1 is a promising candidate for several reasons. 1) IRF7 specifically and directly interacts with DAPK1, as evidenced by tandem-affinity purification experiments with IRF7 as the bait. 2) Moreover, DAPK1 exclusively binds to IRF7 and IRF3 but not with other interferon-dependent proteins such as IRF9, RIG-I or MDA5[30]. These characteristics make DAPK1 an optimal target for indirect yet selective inhibition of IRF7. Accordingly, HS38, a specific DAPK1 inhibitor, was chosen as a potential candidate for a transient inhibition of IRF7 in the current study.

Finally, to validate the concept of NP-based cardio-splenic axis modulation and provide a corresponding nanosystem with clinical translation potential, we designed and constructed a spleen targeting nanosystem termed STEER. The delivery system is composed of erythrocyte-derived materials with simple surface modification of the targeting peptide RP182. With the features of autologous starting materials, simple components and a one-step, green production scheme, the developed STEER NPs showed competitive profiles regarding biosafety and engineering simplicity, which are critical for clinical and industrial translation[49,50]. When loaded with HS38, STEER-HS38 showed superior splenic IRF7 inhibition capacity compared to an FDA-approved nano-micelles formulation, resulting in a substantial cardiac IRF7 inhibition and a reduction in acute myocardial apoptosis during the acute stage of reperfusion challenge. STEER-HS38 preconditioning successfully induced transient inhibition of IRF7 without interfering with subsequent IRF7 expression at 3 days post-IR. This tailored, temporally defined nanotherapy improved the long-term prognosis of myocardial reperfusion injury, as reflected by preserved cardiac function, a reduced fibrotic area and ameliorated cardiac remodeling, verifying the lasting cardioprotective effects of the currently proposed strategy.

In summary, we have demonstrated that NPs sequestered in the spleen can be reutilized as an alternative therapeutic regimen for teleconditioning myocardial reperfusion injury. The approach proposed herein opens new avenues for the development of NP-based interventions for cardiovascular diseases, and the methods generated may provide insights into nanomedicine design for other types of diseases, particularly those previously considered challenging to target directly. Further efforts should be made to explore the transferability of such strategies to wider types of sterile inflammation to advance nanomedicine applications in the field of inflammatory disorders, and continuous efforts to increase the targeting specificity for the spleen will maximize the therapeutic efficacy of such strategies.

Methods

Animals

All animal experiments were carried out in accordance with the requirements of the Institutional Animal Care and Use Committee (IACUC) of Shanghai Jiao Tong University (Approval No. A2024099). Male C57BL/6 J mice were purchased from Zhejiang Charles River Laboratories. ROSA$^{mT/mG}$ mice and IRF7$^{-/-}$ mice on a C57BL/6 J background were purchased from Shanghai Model Organisms Center. Six- to eight-week-old Wistar rats were purchased from Xiamen University Laboratory Animal Center. Animals were housed at a constant temperature of 22 ± 2 °C and relative humidity of 50 ± 10%, under a 12-hour light/dark cycle, and were provided with standard laboratory chow and water ad libitum.

Heterotopic spleen transplantation

The spleen from ROSA$^{mT/mG}$ mice was harvested following a modified version of a previously described procedure[51]. First, mice were anesthetized with isoflurane inhalation and placed in a supine position. The abdominal fur was shaved, and a midline vertical skin incision was made from the pubis to the xiphoid. The intestines were gently moved to the right flank of the abdominal cavity to expose the spleen. The gastric vein attached to the spleen was cauterized using an electrocoagulation pen (Fig. S1b). The esophagus, along with the left gastric vein, was ligated and cut (Fig. S1c). The stomach was repositioned to the right flank of the

abdominal cavity to fully expose the portal vein (Fig. S1d). Branches of the portal vein were ligated (Fig. S1e). The spleen and pancreas were carefully flipped to the right side to expose the abdominal aorta and celiac trunk, along with the splenic artery (Fig. S1f). A total of 200 IU of heparin was injected into the portal vein to prevent clotting throughout the body. Subsequently, the portal vein, along with the splenic vein, spleen, pancreas, and aortic-celiac-splenic artery, was transected. The spleen graft was preserved in 4 °C saline before transplantation.

The spleen graft from the ROSA$^{mT/mG}$ mouse was transplanted into a C57BL/6 J mouse using the cuff technique (Fig. S1a). The recipient mouse was anesthetized with isoflurane inhalation and placed in a supine position. The fur around the neck was shaved, and a midline vertical skin incision was made from the pre-sternum to the lower jaw. The right submaxillary salivary gland was ligated and excised (Fig. S1g). The right external jugular vein was isolated, and its branches were cut (Fig. S1h). The external jugular vein was ligated and cut off at the distal end, and then pulled through the vein cuff. The vessel wall was everted over the cuff and secured using 8-0 silk suture (Fig. S1i). A similar procedure was performed on the right carotid artery (Fig. S1j). Subsequently, the aortic lumen of the spleen graft was wrapped around the aortic cuff and secured using 8-0 silk suture. The portal vein lumen was wrapped around the vein cuff and secured in the same manner. The clamps on the jugular vein and carotid artery were then released (Fig. S1k). The spleen graft was placed into the subcutaneous space, and the incision was sutured.

Isolation and culture of BMDMs

BMDMs were isolated from male C57BL/6 J mice and IRF7(−/−) mice as previously described[52]. In brief, six- to eight-week-old mice were euthanized by carbon dioxide inhalation and treated with 70% ethanol. Skin was removed, and lower limbs were exposed. Tendons and major muscles around the femurs and tibias were removed. The epiphyses were then removed, and the marrow cavities were washed using a 15 ml syringe with 10 ml of PBS. The cell pellet was resuspended in red blood cell lysis buffer for 3 min on ice to remove red blood cells. The isolated bone marrow cells were resuspended in BMDM culture medium (DMEM supplemented with 10% fetal bovine serum, 1% penicillin-streptomycin, and 50 ng/ml M-CSF (MCE, HY-P7085)) and seeded in 12-well culture plates (Corning Costar). Half of the bone marrow culture medium was replaced on day 4. On day 7, fresh bone marrow stimulation medium (DMEM supplemented with 10% fetal bovine serum, 1% penicillin-streptomycin, and 500 ng/ml LPS) was applied for 24 h to activate M1 and M2 phenotypes.

Cell lines and culture

RAW 264.7 cells (TIB-71) and THP-1 cells (TIB-202) were purchased from the American Type Culture Collection (ATCC), and AC16 cells were obtained from Servicebio (STCC13101P). RAW 264.7 and AC16 cells were cultured in DMEM supplemented with 10% fetal bovine serum and 1% penicillin-streptomycin. THP-1 cells were cultured in RPMI 1640 supplemented with 10% fetal bovine serum and 1% penicillin-streptomycin. To differentiate THP-1 cells into macrophages, 100 ng/ml phorbol 12-myristate 13-acetate (PMA, MCE) was used for 48 h. To produce hypoxic-reoxygenation conditioned media from AC16 cells, the cells were treated with 4 μM sodium hydrosulfite (Innochem) for 60 min to induce hypoxia. After thorough rinsing with PBS three times, the cells were returned to normoxic conditions by culturing in regular medium for 4 h. The resulting supernatant was harvested as the hypoxic-reoxygenation conditioned media.

Myocardial IR procedures

Surgical induction of myocardial IR was performed as previously described[53]. In brief, six- to eight-week-old male mice were first anesthetized by isoflurane inhalation and subjected to mechanical ventilation. Hair was removed, and the chest was opened via a left thoracotomy at the 2nd intercostal space. The pericardium was removed, and the left anterior descending artery was ligated with 8-0 silk suture. Ischemia was induced for 60 min before reperfusion. After 24 h of reperfusion, whole blood was collected (heparin was used as an anticoagulant) and centrifuged for 15 min at 1500 × g to obtain serum. Serum LDH1 was measured using a kit from Changchun HUILI Biotech (C028). Area-at-risk and infarct size after 24 h of reperfusion were determined using TTC/Alcian blue staining, as previously described[54]. There were no recorded instances of animal mortality resulting from infarction during the 60-minute IR model. All animals included in the study survived the experimental procedure. Free HS38 (dispersed in 2% F68) or STEER-HS38 at an HS38 concentration of 3.5 mg/kg were intravenously injected at 1 h prior to the myocardial IR process.

Fluorescence migration protocol

To observe the migration of the fluorescent signal from the spleen to the heart, we initially injected 100 μL of 100 μM DiD over three regions of the spleen. The mice were then subjected to 60 min of myocardial ischemia followed by 24 h of reperfusion. Afterward, the mice were euthanized, and both the spleen and heart were harvested and imaged using the IVIS Spectrum CT (In Vivo Imaging System, PerkinElmer).

Flow cytometry

Single-cell suspensions were obtained from heart, spleen, blood and bone marrow, as previously described[55]. In brief, 500ul of blood was collected via heart puncture using heparin as anticoagulant. Red blood cells were removed using red blood cell lysis buffer for 3 min. Bone marrow cells were collected by flushing the marrow cavity of unilateral tibia and fibula using 10 ml of cold PBS. Heart was perfused using 30 ml of cold PBS and dissected using scissors, and digested in DMEM containing 2 mg/ml type IV collagenase (Basal media), 2.4 mg/ml dispase II (Sigma-Aldrich) and 100U/ml DNase I (Servicebio) for 45 min at 37 °C with gentle agitation. Spleen was digested in DMEM containing 1 mg/ml type I collagenase (Basal media), 60U/ml Hyaluronidase (Yeasen Biotechnology) and 100U/ml DNase I for 30 min at 37 °C with gentle agitation. Following digestion, suspensions were passed through a 70-um nylon mesh (BD Falcon), washed and centrifuged. Subsequently, suspensions were incubated with a mixture of antibodies (Supplementary Table 2) at 4 °C for 30 min. Data were acquired on a CytoFLEX Flow Cytometer (Beckman Coulter) and analyzed with FlowJo software (Tree Star). The gating strategy was illustrated in (Supplementary Fig. 26). Initial gating was performed on the forward scatter (FSC) and side scatter (SSC) plot to exclude debris. From the total cell population, live cells were gated using a viability dye to exclude dead cells. Monocytes were identified as CD45 + CD11b + Ly6G-Ly6c$^{low\ to\ high}$, neutrophils were identified as CD45 + CD11b + Ly6G+, T cells were identified as CD45 + CD11b-CD3+, B cells were identified as CD45 + CD11b-B220+, NK cells were identified as CD45 + CD11b-NK1.1+, DCs were identified as CD45 + CD11b-CD11c+MHC II+.

In vivo peptide phage playoff

The in vivo peptide-phage playoff procedure was conducted according to our previously published methodology[34]. The peptide sequences in the playoff pool are presented in the Supplementary Table 3. Briefly, the process is composed with cloning, amplifying, and purifying the peptide-phage clones, followed by determining the titer of the peptide-phage clones. An equimolar phage mix in PBS was prepared, reaching a final titer of 5×10^{10} pfu/ml. Subsequently, the input phage pool was analyzed using high-throughput sequencing to define the library composition at the onset of the experiment. Subsequently, 100 μl of the equimolar phage mix (5×10^9 pfu) was intravenously injected into mice ($n = 3$). After 30 min, the animals were anesthetized, followed by perfusion with PBS. The livers and spleens were dissected, weighed, and placed into 14 ml snap-cap

tubes with 1 ml of LB/NP40. The tissues underwent homogenization, and the phage quantity within each tissue was determined through titration. Subsequently, phages were amplified in tissue lysates and purified through PEG8000 precipitation. Phage pools obtained from the liver and spleen were subjected to high-throughput sequencing analysis. The playoff results were converted into reads per peptide in each sample using the T7 Phage Display Peptide Mining Tool, which is accessible online at http://canbio.ut.ee/. The spleen targeting index for each peptide was calculated by dividing the total reads per peptide in the spleen by the corresponding total reads per peptide in the liver.

Preparation of nano-erythrosomes, STEER-HS38 and DiD-, DiO- and fluorescein- labeled STEER NPs

RBC vesicles were prepared as previously described[56]. Whole blood from C57BL/6 J mice was collected via heart puncture using a syringe containing a heparin solution. The blood was centrifuged at 1500 × *g* for 15 min to remove serum and white blood cells. The packed RBCs were washed with PBS and suspended in lysis buffer at 4 °C for 30 min. The lysates were centrifuged at 10,000 *g* for 5 min repeatedly to remove hemoglobin and suspended in ddH_2O containing 0.2 uM EDTA. Membrane protein concentrations were measured using a BCA kit. To fabricate nano-erythrosomes, the RBC membrane was sonicated for 2 min in a bath sonicator (KQ-500DE, Kunshan ultrasonic instruments) at a frequency of 40 kHz and a power of 200 W. To fabricate STEER NPs, 10 μL of 10 mg/mL RP182 was preincubated with 100 μg of nano-erythrosomes and sonicated. To fabricate STEER-HS38, 20 μL of 10 mM HS38 (HY-15847, MCE) and 10 μL of 10 mg/mL RP182 were preincubated with 100 μg of nano-erythrosomes for 10 min and sonicated. The nanoparticle size was measured by dynamic light scattering (Malvern Panalytical). To fabricate DiD- or DiO-labeled STEER nanoparticles, 20 μL of 1 mM DiD, DiO or fluorescein was preincubated with 100 μg of RBC membrane at 4 °C for 10 min. Subsequently, the mixture was centrifuged at 10000 g for 5 min to remove unbound fluorophores. Following this, 10 μL of 10 mg/mL RP182 was incubated with the fluorescently labeled RBC membrane and sonicated.

HS38 concentration measurement

The concentration of HS38 was evaluated by high performance liquid chromatography (HPLC). The HPLC system was equipped with a C18 column (Supelco Discovery). The mobile phase consisted of acetonitrile and H_2O (v/v, 40/60), with a flow rate set at 1 mL/min. The detection of the HS38 was carried out using a UV detector, set at a wavelength of 300 nm with the reference wavelength of 360 nm. The total run time per analysis was 8 min, and the retention time for HS38 was 4.18 min. To analyze the HS38 concentration in STEER-HS38 NPs, 100 uL previously fabricated STEER-HS38 NPs was dispersed in 900 uL acetonitrile, followed by tip-sonication for 30 s. The sample was further subjected to centrifugation (10,000 *g*, 5 min) and the supernatant was collected for HPLC analysis to quantify the loading degree of HS38.

Pharmacokinetic tests and organ distribution of free HS38 and STEER-HS38

Free HS38 (dispersed in 0.5% or 2% F68, w/v) or STEER-HS38 were i.v. injected to Wistar rat at the HS38 concentration of 1.75 mg/kg. Blood samples were separately collected at 0.08, 0.25, 0.5, 1, 2, 4, 8, 12 and 24 h post injection. The concentration of HS38 in plasma was determined using triple quadrupole liquid chromatography coupled with mass spectrometry (LC-TQ-MS, Agilent 6460). The pharmacokinetic parameters, including maximum concentration (C_{max}), time to reach maximum concentration (T_{max}), half-life ($t_{1/2}$), and area under the curve (AUC), were calculated using non-compartmental analysis through the software DAS (Version 3.0, Chinese Pharmacological Society, China). To evaluate the organ distribution, Free HS38 (dispersed in 2% F68, w/v) or STEER-HS38 were i.v. injected to Wistar rat at an HS38 concentration of 1.75 mg/kg. Major organs including the liver, spleen, kidneys, and heart were harvested at 1 h post injection, and the concentrations of HS38 were quantified through LC-TQ-MS (Agilent 6460).

TEM and EDX elemental mapping

TEM was utilized for the ultrastructural analysis of different NPs. Samples were prepared by depositing a drop of the NP suspension on a carbon-coated copper grid, followed by negative staining with 2% phosphotungstic acid. The grid was then loaded into the TEM for imaging. High-resolution images were captured using a JEM-2100F TEM at an accelerating voltage of 200 kV. Additionally, to identify the elemental composition of the NPs, EDX spectroscopy was performed in conjunction with TEM equipped with an X-MaxN 80 T energy-dispersive X-ray spectrometer. EDX mapping was performed at 200 kV TEM beam voltage. EDX spectral images were acquired with frame-by-frame drift correction using AZtecTEM.

Real-time qPCR

Total RNA was extracted from tissues or cells using a MolPure® TRIeasy™ Plus Total RNA Kit (Yeasen Biotechnology). Complementary DNA was synthesized using a cDNA Synthesis Kit (Yeasen Biotechnology). Real-time qPCR was conducted with a Hieff® qPCR SYBR Green Master Mix and analyzed using Applied Biosystems 7500 (Thermo). All primers for qPCR reactions are listed in Supplementary Table 4.

Western blot

Western blot analysis was conducted following established protocols[56]. Cells were lysed using RIPA lysis buffer (P0013B, Beyotime), supplemented with a protease and phosphatase inhibitor cocktail (P1045, Beyotime). Protein concentrations were determined using the bicinchoninic acid assay (ZJ102, EpiZyme). The protein solutions were mixed with 4X LDS Sample Buffer (Biofuraw™), heated at 95 °C for 10 min, and then subjected to gel electrophoresis on 4–20% bis-tris gels (180-8005HB, Biofuraw™) using MOPS running buffer (BT8100, Biofuraw™). Subsequently, proteins were transferred onto polyvinylidene difluoride membranes (IPVH00010, Millipore) using transfer buffer (8006-6006, Biofuraw™). After blocking with an appropriate blocking solution (P0252FT, Beyotime), the membranes were incubated overnight at 4 °C with primary antibodies (listed in Supplementary Table 2). Following thorough washing, membranes were exposed to secondary antibodies at room temperature for 1 h. Protein bands were detected using the Tanon 4200 Image Analyzer and quantified using the Image J Software (NIH, version 1.52).

Histology and immunohistochemistry

Primary antibodies used for immunohistochemistry are listed in Supplementary Table 2. For histological analysis, mice were euthanized using CO_2 inhalation. The chest was opened, and the heart was flushed with a cold cardioplegia solution (1 M KCl in 1× PBS). The left atrium was incised to facilitate blood drainage, and mice underwent a brief perfusion with cold fixative (4% paraformaldehyde in sodium phosphate buffer, pH 7.4) through the heart apex. Heart tissues were fixed in 4% formalin at room temperature and subsequently embedded in paraffin. Picrosirius red staining was conducted using a staining kit (ab245887), and Masson trichrome staining was performed with a kit from Service Bio (G1006) following the manufacturer's instructions. Fibrosis was quantified as the percentage of picrosirius red-stained or Masson's trichrome blue-stained area over the total tissue area analyzed using image J. For immunofluorescence

staining, slides were blocked in 3% BSA for 30 min, followed by overnight incubation with the primary antibody at 4 °C, washing three times for 5 min in PBS, and subsequent incubation with the secondary antibodies at room temperature for 45 min. The slides were then stained with DAPI.

Echocardiography

Transthoracic echocardiography was conducted using the Vevo 3100 instrument (FUJIFILM VisualSonics) equipped with an MX550D imaging transducer, as previously described[56]. Mice were lightly anesthetized with isoflurane, and chest hair was removed. Throughout the echocardiographic examination, the heart rate was maintained at approximately 500 beats per minute for all mice. Echocardiographic data, including parameters such as left ventricular end-systolic diameter (LVESD), left ventricular end-diastolic diameter (LVEDD), left ventricular end-systolic volume (LVESV), left ventricular end-diastolic volume (LVEDV), left ventricular ejection fraction (LVEF), and left ventricular fractional shortening (LVFS) obtained through M-mode assessments, were collected and analyzed using VevoLAB software (VisualSonics) on both day 7 and day 42.

ELISA

To determine the levels of cytokines in the supernatant of BMDM cells, the cell culture medium was collected and centrifuged at 1500 × *g* for 10 min at 4 °C to obtain the supernatant. The ELISA assays for IFN-b, CXCL10, and IL-6 (MULTISCIENCES) were conducted following the manufacturer's protocol. To determine myocardial cytokine levels, 50–60 mg of the left ventricle was homogenized in Tissue Extraction Reagent I (Invitrogen) supplemented with 1 mM PMSF and Protease Inhibitor cocktails. The homogenate was centrifuged at 12,000 g for 20 min at 4 °C, and the resulting supernatant was collected. Protein concentrations were determined using the Protein Assay with BSA as the standard curve. Subsequently, samples were aliquoted and stored at −80 °C for subsequent ELISA analysis. The IFN-b ELISA (MULTISCIENCES) and IL-6 ELISA (ServiceBio) were performed according to the manufacturer's protocol. Cytokine values were normalized to protein content and expressed as picograms per milligram of protein.

To evaluate the impact of temporary IRF7 inhibition by STEER-HS38 on the antiviral immune response, male C57BL/6 mice aged 8 weeks were randomly assigned to two groups. The treatment group received a single intravenous injection of STEER-HS38 at an HS38 concentration of 3.5 mg/kg via the tail vein. The control group was administered an equivalent volume of sterile phosphate-buffered saline (PBS). One hour after STEER-HS38 administration, both groups were injected intraperitoneally with 10 μg of polyinosinic-polycytidylic acid (poly(I:C); MCE, HY-107202) dissolved in sterile ddH_2O to simulate a viral infection. Seven days post-injection, mice were euthanized, and whole blood was collected via cardiac puncture. Serum was separated by centrifugation at 1500 *g* for 10 min at 4 °C and stored at −80 °C until analysis. Serum levels of IgM and IgG were measured using ELISA kits (Elabscience, E-EL-M3036 & E-EL-M0692) following the manufacturer's instructions.

Isolation of human monocytes

Isolation of monocytes was carried out using whole blood obtained from patients who experienced acute myocardial infarction and subsequently underwent PCI for coronary artery revascularization in Shanghai Jiao Tong University School of Medicine affiliated Ruijin Hospital, with approval from the Ruijin Hospital Ethics Committee, Shanghai Jiao Tong University School of Medicine. Isolation of human monocytes was performed with written informed consent obtained from all involved subjects or their agents. Blood samples were collected twice from each patient: the first draw occurred upon the patient's arrival at the emergency department of Ruijin Hospital, and the second draw took place approximately 4 h after PCI. Human peripheral blood mononuclear cells (PBMCs) were isolated from the blood samples using a lymphocyte separation medium (Yeasen Biotechnology), following the manufacturer's protocol. Briefly, 2 ml of whole blood was initially diluted with 2 ml of PBS and carefully layered on top of 3 ml of lymphocyte separation medium in a 15 ml centrifuge tube. The resulting mixture was centrifuged at 400 *g* for 30 min. Subsequently, the PBMC layer was carefully extracted and subjected to a PBS wash. Subsequently, PBMCs were subjected to CD14 magnetic separation (Miltenyi Biotec), ensuring the specific isolation of monocytes from each patient's blood sample.

Single-cell RNA-seq

The scRNA-seq experiment was performed by Shanghai OE Biotech, using the Chromium Next GEM Single Cell 3′ Reagent Kits v3.1, following the protocols outlined in the manufacturer's guidelines. Briefly, single cells were encapsulated into Gel Beads in Emulsion (GEMs), with each bead containing a unique barcode sequence. Reverse transcription of cellular RNA captured poly(A)-tailed mRNA, converting it into cDNA while incorporating unique molecular identifiers (UMIs) for precise quantification. Subsequent cDNA amplification and library preparation involved a ligation step, introducing specific adapters for downstream sequencing. The resulting cDNA libraries were sequenced using Nextera sequencing technology, generating high-quality paired-end reads. The obtained raw sequencing data were then subjected to preprocessing using the Cell Ranger software pipeline (version 5.0.0) provided by 10×Genomics. This included the demultiplexing of cellular barcodes, mapping of reads to the relevant genome and transcriptome using the STAR aligner, and necessary read downsampling to ensure balanced data across samples. The outcome was a count matrix representing the expression levels of genes in individual cells. Cells were filtered based on UMI counts per gene, and cells with UMI/gene numbers beyond the median value ± 2-fold of the median absolute deviation were excluded. Additionally, cells with more than 10% mitochondrial gene expression were considered of low quality and excluded from subsequent analyses. Further analyses involved library size normalization using Seurat's NormalizeData function and the identification of top variable genes through the FindVariableGenes function. Principal component analysis (PCA) and graph-based clustering were performed to reduce dimensionality and categorize cells based on their gene expression profiles. Visualization was accomplished using the Uniform Manifold Approximation and Projection (UMAP) algorithm, implemented through Seurat's RunUMAP function. Marker genes for individual clusters were identified utilizing the FindAllMarkers function. Furthermore, the SingleR computational method was applied to unbiasedly infer cell types using reference transcriptomic dataset. Differentially expressed genes (DEGs) were identified using the FindMarkers function, with significance thresholds set at a p-value < 0.05 and log2 fold change > 0.58. Enrichment analyses for gene ontology (GO) terms and KEGG pathways were conducted using the clusterProfiler package. For single-cell trajectory analysis, we used Monocle v.2.4.0 to investigate developmental trajectories between macrophage/monocyte subsets[57].

RNA-seq analysis

The RNA-seq experiment was performed by Shanghai OE Biotech, as previously described[56]. Total RNA was isolated from each sample using the Trizol reagent (Invitrogen) and assessed for quality using an Agilent 2200 system. Subsequently, cDNA libraries were prepared for each RNA sample using the TruSeq Stranded mRNA Library Prep Kit (Illumina, Inc.) following the manufacturer's protocols. Library quality was confirmed using an Agilent 2200 system, and sequencing was performed on a 150-bp paired-end run with a Hiseq XTen instrument. Clean reads were aligned to the mouse genome (GRCm38, NCBI) using Hisat2 software. Gene counts were obtained utilizing HTseq, and gene expression levels were determined employing the RPKM

technique. For gene set enrichment analysis (GSEA), GSEA version 4.1.0 software (Broad Institute) was utilized. Statistical significance was assessed through 10000 random permutations of the gene set with a signal-to-noise metric for gene ranking. A false discovery rate (FDR)-corrected value of $q < 0.25$ was considered significant. Gene sets were sourced from the Molecular Signatures Database (MSigDB) version 7.4.

Adoptive transfer of mice IR serum

Mice were subjected to the IR surgical procedures as outlined earlier. Following 1 h of reperfusion, mice were euthanized, and 500 µL of blood was collected via cardiac puncture. The blood was then centrifuged at 1500 × *g* for 15 min to isolate serum. For the heat-inactivation group, serum was incubated at 56 °C for 30 min. In the DNase-treated group, 5U of DNase I (Servicebio) was added to the serum and incubated at 37 °C for 10 min. In the RNase-treated group, 5U of RNase A (Servicebio) was added to the serum and incubated at room temperature for 30 min. After the respective treatments, the treated serum was intravenously administered to healthy mice. One hour following administration, the spleens were harvested, and total mRNA was extracted for further analysis.

Statistics and reproducibility

The data are graphically presented using bar plots, indicating mean values with corresponding standard deviations (mean ± s.d.). The specific "n" values for each experiment can be found in the figure legends or directly annotated on the figures. Significant differences between the two groups were assessed utilizing a two-tailed Student's *t*-test. For comparisons involving more than two groups, a one-way ANOVA followed by Tukey's post hoc test was employed. In all analyses, a significance threshold of $P < 0.05$ was applied to determine statistical significance.

Reporting summary

Further information on research design is available in the Nature Portfolio Reporting Summary linked to this article.

Data availability

All data supporting the findings of this study are available within the paper and its supplementary information files. Source data are provided with this paper. Raw single cell RNA sequencing data were deposited in the GEO under accession number GSE282100. Source data are provided with this paper.

Code availability

All the codes used in this study are open source and are accessible to the public. The R packages used are indicated in the Methods.

References

1. Smith, B. R. & Edelman, E. R. Nanomedicines for cardiovascular disease. *Nat. Cardiovasc. Res.* **2**, 351–367 (2023).
2. Mitchell, M. J. et al. Engineering precision nanoparticles for drug delivery. *Nat. Rev. Drug Discov.* **20**, 101–124 (2021).
3. Liu, Z. et al. Promoting cardiac repair through simple engineering of nanoparticles with exclusive targeting capability toward myocardial reperfusion injury by thermal resistant microfluidic platform. *Adv. Funct. Mater.* **32**, 2204666 (2022).
4. Shin, M. et al. Targeting protein and peptide therapeutics to the heart via tannic acid modification. *Nat. Biomed. Eng.* **2**, 304–317 (2018).
5. Fish, M. B. et al. Deformable microparticles for shuttling nanoparticles to the vascular wall. *Sci. Adv.* **7**, eabe0143 (2021).
6. Dasa, S. S. K. et al. Development of target-specific liposomes for delivering small molecule drugs after reperfused myocardial infarction. *J. Control Release* **220**, 556–567 (2015).
7. Tsoi, K. M. et al. Mechanism of hard-nanomaterial clearance by the liver. *Nat. Mater.* **15**, 1212–1221 (2016).
8. Smith, B. R. Nanotherapeutics for cardiovascular disease. *Nat. Rev. Cardiol.* **18**, 617–618 (2021).
9. Myerson, J. W. et al. Supramolecular arrangement of protein in nanoparticle structures predicts nanoparticle tropism for neutrophils in acute lung inflammation. *Nat. Nanotechnol.* **17**, 86–97 (2022).
10. Luo, Z. et al. Neutrophil hitchhiking for drug delivery to the bone marrow. *Nat. Nanotechnol.* **18**, 647–656 (2023).
11. Huang, S. S. et al. Immune cell shuttle for precise delivery of nanotherapeutics for heart disease and cancer. *Sci. Adv.* **7**, eabf2400 (2021).
12. Flores, A. M. et al. Pro-efferocytic nanoparticles are specifically taken up by lesional macrophages and prevent atherosclerosis. *Nat. Nanotechnol.* **15**, 154–161 (2020).
13. Guilliams, M., Mildner, A. & Yona, S. Developmental and functional heterogeneity of monocytes. *Immunity* **49**, 595–613 (2018).
14. Swirski, F. K. et al. Identification of splenic reservoir monocytes and their deployment to inflammatory sites. *Science* **325**, 612–616 (2009).
15. Heusch, G. Cardioprotection: chances and challenges of its translation to the clinic. *Lancet* **381**, 166–175 (2013).
16. Shi, C. & Pamer, E. G. Monocyte recruitment during infection and inflammation. *Nat. Rev. Immunol.* **11**, 762–774 (2011).
17. Furze, R. C. & Rankin, S. M. Neutrophil mobilization and clearance in the bone marrow. *Immunology* **125**, 281–288 (2008).
18. Fan, Q. et al. Dectin-1 contributes to myocardial ischemia/reperfusion injury by regulating macrophage polarization and neutrophil infiltration. *Circulation* **139**, 663–678 (2019).
19. Terkeltaub, R. et al. Monocyte-derived neutrophil chemotactic factor/interleukin-8 is a potential mediator of crystal-induced inflammation. *Arthritis Rheum.* **34**, 894–903 (1991).
20. Samarajiwa, S. A., Forster, S., Auchettl, K. & Hertzog, P. J. INTERFEROME: the database of interferon regulated genes. *Nucleic Acids Res.* **37**, D852–D857 (2009).
21. Honda, K. et al. IRF-7 is the master regulator of type-I interferon-dependent immune responses. *Nature* **434**, 772–777 (2005).
22. Swirski, F. K. & Nahrendorf, M. Cardioimmunology: the immune system in cardiac homeostasis and disease. *Nat. Rev. Immunol.* **18**, 733–744 (2018).
23. Prabhu, S. D. Healing and repair after myocardial infarction: the forgotten but resurgent basophil. *J. Clin. Invest* **131**, e150555 (2021).
24. Frangogiannis, N. G. The inflammatory response in myocardial injury, repair, and remodelling. *Nat. Rev. Cardiol.* **11**, 255–265 (2014).
25. Lenti, M. V. et al. Asplenia and spleen hypofunction. *Nat. Rev. Dis. Prim.* **8**, 71 (2022).
26. Cohen, M. et al. Chronic exposure to TGFbeta1 regulates myeloid cell inflammatory response in an IRF7-dependent manner. *EMBO J.* **33**, 2906–2921 (2014).
27. Han, H. RNA interference to knock down gene expression. *Methods Mol. Biol.* **1706**, 293–302 (2018).
28. Liu, Z. et al. Non-viral nanoparticles for RNA interference: Principles of design and practical guidelines. *Adv. Drug Deliv. Rev.* **174**, 576–612 (2021).
29. Gao, H. et al. Rational design of a polysaccharide-based viral mimicry nanocomplex for potent gene silencing in inflammatory tissues. *J. Control Release* **357**, 120–132 (2023).
30. Zhang, J., Hu, M. M., Shu, H. B. & Li, S. Death-associated protein kinase 1 is an IRF3/7-interacting protein that is involved in the cellular antiviral immune response. *Cell Mol. Immunol.* **11**, 245–252 (2014).
31. Zhai, Y. et al. A splenic-targeted versatile antigen courier: iPSC wrapped in coalescent erythrocyte-liposome as tumor nanovaccine. *Sci. Adv.* **7**, eabi6326 (2021).

32. Han, X. et al. Red blood cell-derived nanoerythrosome for antigen delivery with enhanced cancer immunotherapy. *Sci. Adv.* **5**, eaaw6870 (2019).
33. Lingasamy, P. & Teesalu, T. Homing peptides for cancer therapy. *Adv. Exp. Med Biol.* **1295**, 29–48 (2021).
34. Posnograjeva, K., Pleiko, K., Haugas, M. & Teesalu, T. New tools for streamlined in vivo homing peptide identification. *Methods Mol. Biol.* **2383**, 385–412 (2022).
35. Jaynes, J. M., Lopez, H. W., Martin, G. R., Yates, C., & Garvin, C. E. Peptides having anti-inflammatory properties. US Patent 9,492,499 B2 (2016).
36. DeWitt, E. S. et al. Effects of commonly used inotropes on myocardial function and oxygen consumption under constant ventricular loading conditions. *J. Appl Physiol. (1985)* **121**, 7–14 (2016).
37. Sahoo, S., Kariya, T. & Ishikawa, K. Targeted delivery of therapeutic agents to the heart. *Nat. Rev. Cardiol.* **18**, 389–399 (2021).
38. Lewis, S. M., Williams, A. & Eisenbarth, S. C. Structure and function of the immune system in the spleen. *Sci. Immunol.* **4**, eaau6085 (2019).
39. Kaur, S., Allan, S. M. & Al-Ahmady, Z. S. Re-directing nanomedicines to the spleen: A potential technology for peripheral immunomodulation. *J. Control Release* **350**, 60–79 (2022).
40. Leuschner, F. et al. Rapid monocyte kinetics in acute myocardial infarction are sustained by extramedullary monocytopoiesis. *J. Exp. Med.* **209**, 123–137 (2012).
41. Hoang, A. C. et al. Mitochondrial RNA stimulates beige adipocyte development in young mice. *Nat. Metab.* **4**, 1684–1696 (2022).
42. Ning, S., Pagano, J. S. & Barber, G. N. IRF7: activation, regulation, modification and function. *Genes Immun.* **12**, 399–414 (2011).
43. King, K. R. et al. IRF3 and type I interferons fuel a fatal response to myocardial infarction. *Nat. Med.* **23**, 1481–1487 (2017).
44. Tanaka, T., Murakami, K., Bando, Y. & Yoshida, S. Interferon regulatory factor 7 participates in the M1-like microglial polarization switch. *Glia* **63**, 595–610 (2015).
45. Chen, L. et al. NF-kappaB p65 and SETDB1 expedite lipopolysaccharide-induced intestinal inflammation in mice by inducing IRF7/NLR-dependent macrophage M1 polarization. *Int Immunopharmacol.* **115**, 109554 (2023).
46. Yang, X. et al. Repolarizing heterogeneous leukemia-associated macrophages with more M1 characteristics eliminates their pro-leukemic effects. *Oncoimmunology* **7**, e1412910 (2018).
47. Jung, S. H. et al. Spatiotemporal dynamics of macrophage heterogeneity and a potential function of Trem2(hi) macrophages in infarcted hearts. *Nat. Commun.* **13**, 4580 (2022).
48. Puthia, M. et al. IRF7 inhibition prevents destructive innate immunity-A target for nonantibiotic therapy of bacterial infections. *Sci. Transl. Med.* **8**, 336ra359 (2016).
49. Liu, Z., Fontana, F., Python, A., Hirvonen, J. T. & Santos, H. A. Microfluidics for production of particles: mechanism, methodology, and applications. *Small* **16**, e1904673 (2020).
50. Liu, Z. et al. Multifunctional nanohybrid based on porous silicon nanoparticles, gold nanoparticles, and acetalated dextran for liver regeneration and acute liver failure theranostics. *Adv. Mater.* **30**, e1703393 (2018).
51. Wang, J. J. et al. A mouse model of vascularized heterotopic spleen transplantation for studying spleen cell biology and transplant immunity. *J. Vis. Exp.* **148**, e59616(2019).
52. Toda, G., Yamauchi, T., Kadowaki, T. & Ueki, K. Preparation and culture of bone marrow-derived macrophages from mice for functional analysis. *STAR Protoc.* **2**, 100246 (2021).
53. Vagnozzi, R. J. et al. An acute immune response underlies the benefit of cardiac stem cell therapy. *Nature* **577**, 405–409 (2020).
54. Zhang, T. et al. CaMKII is a RIP3 substrate mediating ischemia- and oxidative stress-induced myocardial necroptosis. *Nat. Med.* **22**, 175–182 (2016).
55. Krohn-Grimberghe, M. et al. Nanoparticle-encapsulated siRNAs for gene silencing in the haematopoietic stem-cell niche. *Nat. Biomed. Eng.* **4**, 1076–1089 (2020).
56. Long, Q. et al. Autologous skin fibroblast-based PLGA nanoparticles for treating multiorgan fibrosis. *Adv. Sci.* **9**, e2200856 (2022).
57. Trapnell, C. et al. The dynamics and regulators of cell fate decisions are revealed by pseudotemporal ordering of single cells. *Nat. Biotechnol.* **32**, 381–386 (2014).

Acknowledgements

X.Y. acknowledges financial support from the National Science Foundation for Distinguished Young Scholars of China (82125019), Program of Shanghai Municipal Health Commission (202140184; 2022JC028), Program of Shanghai Academic (22S31905000;201409005400), Shanghai Jiao Tong University medical engineering cross project (YG2022ZD002) and the Joint research project of Institute of Biomaterials and Regenerative Medicine, School of Medicine, Shanghai Jiao Tong University (2022LHA10). Q.Z acknowledges financial support from the National Key Research and Development Program of China (2022YFA1105100), National Natural Science Foundation of China (82070429). Z.L. acknowledges financial support from the Academy of Finland (340129) and Finnish Foundation for Cardiovascular Research, H.A.S. acknowledges financial support from the UMCG Research Funds, Q.L. acknowledges financial support from the Shanghai Sailing Program (24YF2726200), S.H. acknowledges financial support from the Youth Fund of the National Natural Science Foundation of China (82100264), "Chen Guang" project supported by Shanghai Municipal Education Commission and Shanghai Education Development Foundation (21CGA17).

Author contributions

Q.L. and Z.L. conceived and designed the study, performed experiments, analyzed data, and wrote the manuscript. K.R. conducted experiments related to the phage library, collected and analyzed data, L.L. (Lihui Li), S.H., B.Q., Y.Z. (Yiming Zhong), Z.Q., W.X., H.J., J.Z., Y.C (Yu Cai)., L.C., H.Z., T.R., Z.W., L.L. (Lin Lu), Z.Z., C.W., and Y.Z. (Yecen Zhang) contributed to study design, data analysis, and manuscript editing. K.H., and X.W. conducted experiments, collected and analyzed data, and assisted in manuscript preparation. Y. C. (Yiwei Chu), T.T., H.A.S., Q.Z. and X.Y. provided critical intellectual input, supervised the research, and revised the manuscript. All authors reviewed and approved the final version of the manuscript. We thank BioRender.com for providing a platform to create the schematics used in figures.

Competing interests

The authors declare no competing interests.

Additional information

Supplementary information The online version contains supplementary material available at https://doi.org/10.1038/s41467-025-57048-6.

Correspondence and requests for materials should be addressed to Zehua Liu, Qiang Zhao or Xiaofeng Ye.

Peer review information *Nature Communications* thanks Thomas Decker, and the other, anonymous, reviewers for their contribution to the peer review of this work. A peer review file is available.

Qiang Long[1], Kristina Rabi[2], Yu Cai[3], Lihui Li[1], Shixing Huang[1], Bei Qian[1], Yiming Zhong[1], Zhaoxi Qi[1], Yecen Zhang[1], Kaichen Huang[1], Xinming Wang[1], Lan Chang[1], Weichang Xie[1], Huaiyu Jiang[1], Haonan Zhang[1], Junjie Zhang[1], Ting Ren[1], Zichen Wang[1], Tambet Teesalu[2], Caisheng Wu[3], Lin Lu[4], Zhengbin Zhu[4], Yiwei Chu[5], Hélder A. Santos[6,7], Zehua Liu[6,7] ✉, Qiang Zhao[1] ✉ & Xiaofeng Ye[1] ✉

[1]Department of Cardiovascular Surgery, Ruijin Hospital, Shanghai Jiao Tong University School of Medicine, Shanghai, China. [2]Laboratory of Precision and Nanomedicine, Institute of Biomedicine and Translational Medicine, University of Tartu, Tartu, Estonia. [3]Fujian Provincial Key Laboratory of Innovative Drug Target Research, School of Pharmaceutical Sciences, Xiamen University, Xiamen, Fujian, China. [4]Department of Cardiovascular Medicine, Ruijin Hospital, Shanghai Jiao Tong University School of Medicine, Shanghai, China. [5]Department of Immunology, School of Basic Medical Sciences, Biotherapy Research Center and Institutes of Biomedical Sciences, Fudan University, Shanghai, China. [6]Drug Research Program, Division of Pharmaceutical Chemistry and Technology, Faculty of Pharmacy, University of Helsinki, Helsinki, Finland. [7]Department of Biomaterials and Biomedical Technology, The Personalized Medicine Research Institute (PRECISION), University Medical Center Groningen, University of Groningen (UMCG), AV Groningen, Netherlands.
✉e-mail: zehua.liu@helsinki.fi; zq11607@rjh.com.cn; xiaofengye@hotmail.com